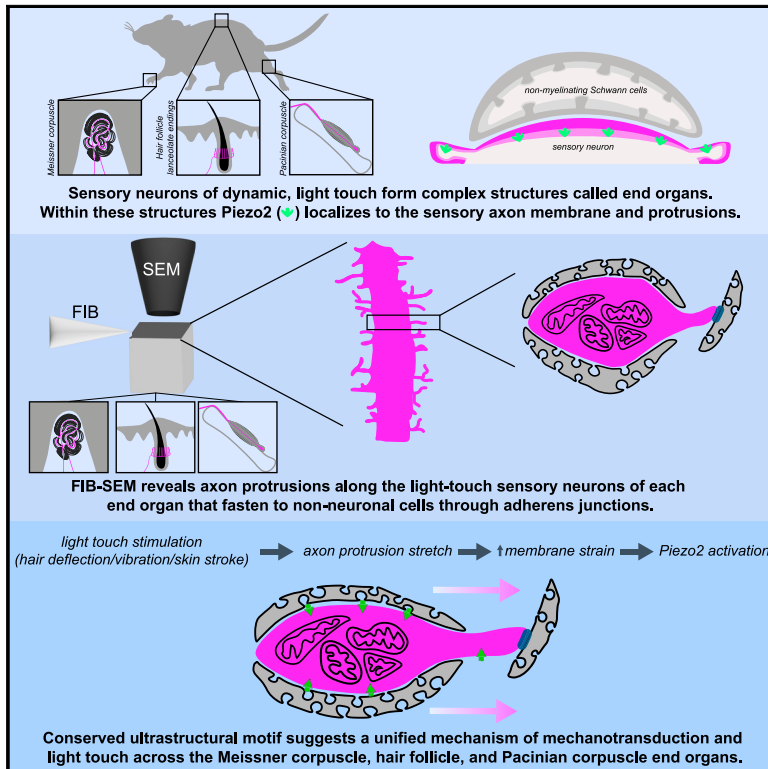


# Three-dimensional reconstructions of mechanosensory end organs suggest a unifying mechanism underlying dynamic, light touch

## Graphical abstract



## Authors

Annie Handler, Qiyu Zhang, Song Pang, ..., Wei-Chung Allen Lee, C. Shan Xu, David D. Ginty

## Correspondence

david\_ginty@hms.harvard.edu

## In brief

Handler, Zhang, et al. show restricted subcellular localization and function of Piezo2 to the sensory axons of mechanosensory end organs, and through high-resolution enhanced FIB-SEM, they reveal a conserved ultrastructural anchoring motif shared by end organs involved in dynamic, light touch. These findings suggest a unified model of mechanotransduction.

## Highlights

- In end organs, Piezo2 is restricted in expression and function to sensory axons
- Enhanced FIB-SEM reveals conserved ultrastructural features shared by distinct A $\beta$  RA-LTMRs
- A $\beta$  RA-LTMRs of each end organ contain a high density of axon protrusions
- Axon protrusions anchor to end organ Schwann cells through adherens junctions



## Article

# Three-dimensional reconstructions of mechanosensory end organs suggest a unifying mechanism underlying dynamic, light touch

Annie Handler,<sup>1,2,7</sup> Qiyu Zhang,<sup>1,2,7</sup> Song Pang,<sup>3,5</sup> Tri M. Nguyen,<sup>1</sup> Michael Iskols,<sup>1,2</sup> Michael Nolan-Tamariz,<sup>1,2</sup> Stuart Cattel,<sup>1,2</sup> Rebecca Plumb,<sup>1,2</sup> Brianna Sanchez,<sup>1,2</sup> Karyl Ashjian,<sup>1,2</sup> Aria Shotland,<sup>1,2</sup> Bartianna Brown,<sup>1,2</sup> Madiha Kabeer,<sup>1,2</sup> Josef Turecek,<sup>1,2</sup> Michelle M. DeLisle,<sup>1,2</sup> Genelle Rankin,<sup>1,2</sup> Wangchu Xiang,<sup>1,2</sup> Elisa C. Pavarino,<sup>1,2</sup> Nusrat Africawala,<sup>1,2</sup> Celine Santiago,<sup>1,2</sup> Wei-Chung Allen Lee,<sup>1,4</sup> C. Shan Xu,<sup>3,6</sup> and David D. Ginty<sup>1,2,8,\*</sup>

<sup>1</sup>Department of Neurobiology, Harvard Medical School, 220 Longwood Avenue, Boston, MA 02115, USA

<sup>2</sup>Howard Hughes Medical Institute, Harvard Medical School, 220 Longwood Avenue, Boston, MA 02115, USA

<sup>3</sup>Janelia Research Campus, Howard Hughes Medical Institute, Ashburn, VA 20147, USA

<sup>4</sup>F.M. Kirby Neurobiology Center, Boston Children's Hospital, Boston, MA, USA

<sup>5</sup>Present address: Yale School of Medicine, New Haven, CT 06510, USA

<sup>6</sup>Present address: Department of Cellular & Molecular Physiology, Yale School of Medicine, New Haven, CT 06510, USA

<sup>7</sup>These authors contributed equally

<sup>8</sup>Lead contact

\*Correspondence: [david\\_ginty@hms.harvard.edu](mailto:david_ginty@hms.harvard.edu)

<https://doi.org/10.1016/j.neuron.2023.08.023>

## SUMMARY

Across mammalian skin, structurally complex and diverse mechanosensory end organs respond to mechanical stimuli and enable our perception of dynamic, light touch. How forces act on morphologically dissimilar mechanosensory end organs of the skin to gate the requisite mechanotransduction channel Piezo2 and excite mechanosensory neurons is not understood. Here, we report high-resolution reconstructions of the hair follicle lanceolate complex, Meissner corpuscle, and Pacinian corpuscle and the subcellular distribution of Piezo2 within them. Across all three end organs, Piezo2 is restricted to the sensory axon membrane, including axon protrusions that extend from the axon body. These protrusions, which are numerous and elaborate extensively within the end organs, tether the axon to resident non-neuronal cells via adherens junctions. These findings support a unified model for dynamic touch in which mechanical stimuli stretch hundreds to thousands of axon protrusions across an end organ, opening proximal, axonal Piezo2 channels and exciting the neuron.

## INTRODUCTION

Our perception of light touch is initiated by the activation of mechanically sensitive low-threshold mechanoreceptors (LTMRs) whose endings in the skin associate with non-myelinating Schwann cells and other cell types to form complex terminal structures called mechanosensory end organs. The cell bodies of these light-touch mechanosensory neurons reside within the dorsal root ganglia (DRG) and trigeminal ganglia and extend a peripherally projecting axon that terminates within a peripheral end organ and a second, centrally projecting axon that extends into the spinal cord and brainstem. Thus, forces generated by tactile stimuli impinging on the skin surface activate the end organs, where mechanical forces are converted to electrical signals that are propagated along the LTMR axon to the spinal cord and brainstem. Although the structural diversity of mechanosensory end organs has been appreciated for nearly two centuries and has long been thought to underlie the distinct tuning

properties of LTMR subtypes,<sup>1</sup> how forces acting on these structurally dissimilar end organs lead to mechanotransduction has remained unclear.

The sensory neurons of touch can be classified based on their electrophysiological properties, including conduction velocity (A $\beta$ -, A $\delta$ -, and C-fiber) and force threshold for activation (low or high threshold). Our sense of discriminative light touch arises predominantly from the fast-conducting, A $\beta$  low-threshold mechanoreceptors (A $\beta$  LTMRs), which are activated by indentation forces as low as 0.5–2 mN.<sup>2–8</sup> The A $\beta$  LTMRs can be subdivided by their rate of adaptation, with slowly adapting (SA) neurons firing throughout the duration of static indentation,<sup>9–12</sup> and rapidly adapting (RA) neurons firing only 1–2 action potentials during the onset and offset of a step indentation.<sup>13,14</sup> A $\beta$  LTMRs are further distinguished by their vibration tuning and receptive field properties. Indeed, in glabrous (non-hairy) skin, there are two distinct A $\beta$  RA-LTMR subtypes that are optimally sensitive to either low-frequency vibrations (40–100 Hz) and



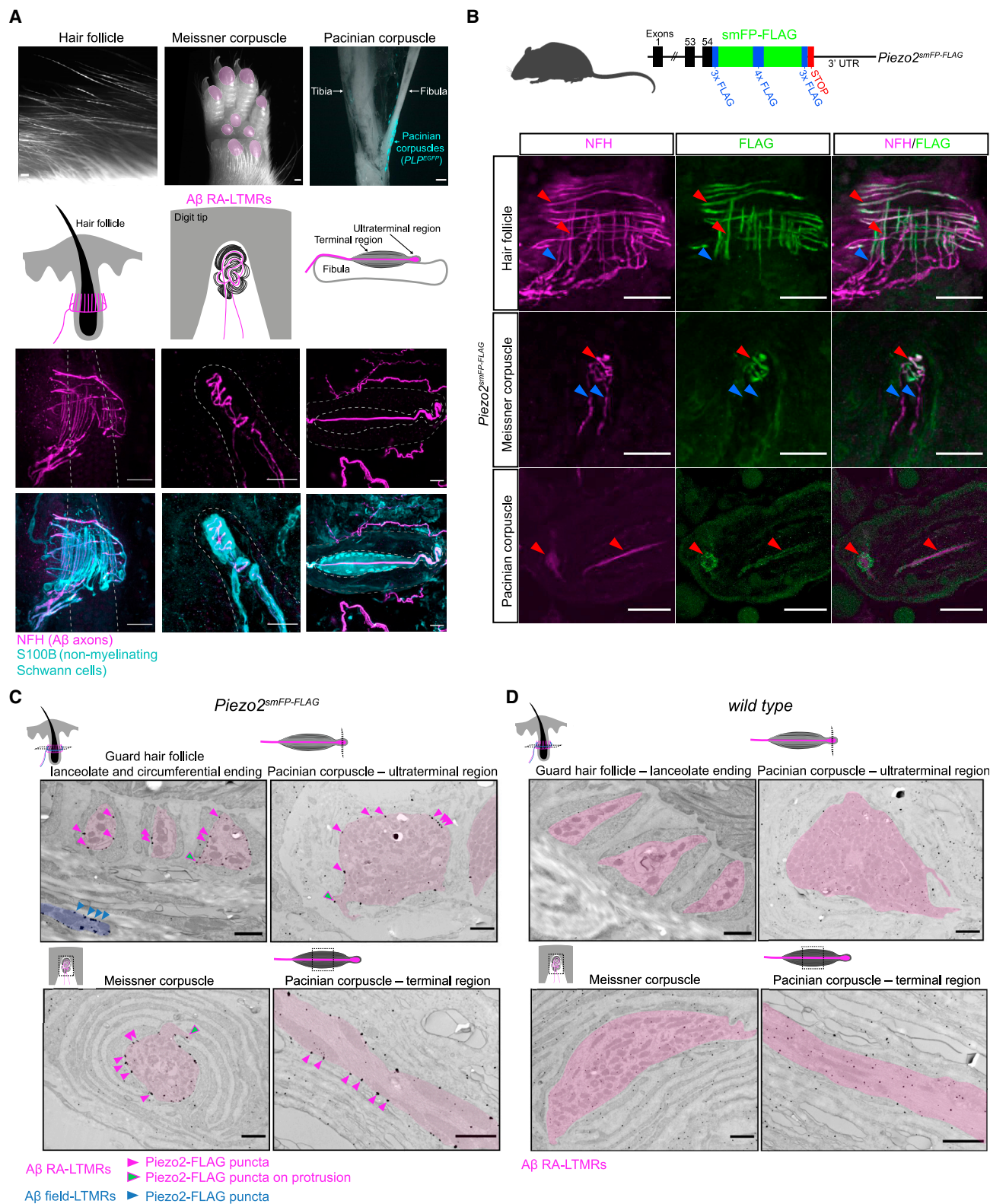


**Figure 1. Piezo2 is restricted to axonal endings across morphologically dissimilar Aβ RA-LTMRs**

(A) Image of three main skin/tissue regions that contain end organs formed by Aβ RA-LTMRs: lanceolate endings around hair follicles, Meissner corpuscles within glabrous skin of digit tips and pedal pads (regions indicated in pink), and Pacinian corpuscles (indicated by the PLP<sup>EGFP</sup> fluorescent label) around the periosteum (legend continued on next page)

exhibit small receptive fields or instead are uniquely sensitive to higher frequencies (>200 Hz) and exhibit expansive receptive fields.<sup>1,3,15–18</sup> This difference in vibration tuning is thought to arise from the dissimilar end organ structures formed by these two A $\beta$  RA-LTMRs subtypes. On the other hand, the A $\beta$  SA-LTMRs of hairy and glabrous skin have small receptive fields, and although A $\beta$  SA-LTMRs are sensitive to vibratory stimuli, these neurons exhibit minimal frequency tuning.<sup>1,18</sup> These distinctions in physiological and receptive field properties of A $\beta$  LTMR subtypes have led to the suggestion that while A $\beta$  SA-LTMRs report pressure, points, and edges within their receptive fields, the A $\beta$  RA-LTMRs are uniquely suited to report dynamic tactile stimuli.

The unique physiological properties of A $\beta$  LTMR subtypes are reflected in their distinct end organ structures. A $\beta$  SA-LTMRs innervate both hairy and glabrous skin types to form Merkel cell-neurite complexes at the dermal-epidermal boundary.<sup>19,20</sup> A $\beta$  RA-LTMR subtypes also innervate both skin types, forming longitudinal lanceolate endings that run parallel to the shaft of hair follicles in hairy skin,<sup>8,21–24</sup> and Meissner corpuscles (low-frequency tuned and small receptive field) and Pacinian corpuscles (high-frequency tuned with a large receptive field) located in glabrous skin or in the deep dermis and associated with bones, respectively.<sup>14,25</sup> Despite the overall distinct morphologies of the A $\beta$  RA-LTMRs associated with hair follicles, Meissner corpuscles, and Pacinian corpuscles (Figure 1A), the observation that the A $\beta$  RA-LTMRs of these three structures are highly sensitive and tuned to vibrotactile stimuli (Figures S1A–S1C) suggests a conserved mechanotransduction mechanism underlying dynamic, light touch. In addition to the ultrasensitive A $\beta$  RA-LTMRs that innervate hair follicles and corpuscles, additional LTMR subtypes that are less sensitive to tactile stimuli also terminate within these structures. This includes A $\beta$  field-LTMRs,<sup>2</sup> which form circumferential endings that wrap around hair follicles distal to the lanceolate complexes, and Ret-positive (Ret<sup>+</sup>) A $\beta$  LTMRs that innervate Meissner corpuscles alongside the more sensitive TrkB-positive (TrkB<sup>+</sup>) A $\beta$  RA-LTMRs.<sup>3</sup> The basis for the varied mechanosensitivity of A $\beta$  LTMR subtypes across distinct end organs and even within the same end organ remains an outstanding question.

Remarkably, despite the wide range of physiological and morphological properties across the mechanosensory neurons, Piezo2 has emerged as the principal, requisite mechanosensitive channel for LTMR subtypes.<sup>26–34</sup> Indeed, mice and humans lacking Piezo2 exhibit profound deficits in light-touch sensation.<sup>26–30,35,36</sup> While the terminal structure of the Merkel cell-neu-

rite complex formed by A $\beta$  SA-LTMRs is relatively simple and the mechanism by which force activates Piezo2 within this complex is well studied,<sup>35–39</sup> the basis for how forces activate Piezo2 in the more complex end organ structures formed by the A $\beta$  RA-LTMR subtypes that underlie dynamic, light touch—including hair follicle lanceolate complexes, Meissner corpuscles, and Pacinian corpuscles—remains unknown. Here, we report large-scale, high-resolution 3D electron microscopy (EM) reconstructions of these three A $\beta$  RA-LTMR end organs and the subcellular distribution of Piezo2 within them. Our findings reveal a unified model of mechanotransduction within the mechanosensory end organs of dynamic, light touch.

## RESULTS

### Piezo2 localization across three A $\beta$ RA-LTMR end organ structures

We first localized Piezo2 within the end organs innervated by A $\beta$  RA-LTMRs—the guard hair follicle, Meissner corpuscle, and Pacinian corpuscle. We generated a knockin mouse in which a “spaghetti monster-FLAG” (smFP-FLAG) epitope tag<sup>40</sup> is fused to the carboxy terminal end of the Piezo2 protein (*Piezo2*<sup>smFP-FLAG</sup> mice; Figure 1B) to enable specific, high-affinity immuno-localization of endogenous Piezo2. The multimerized FLAG epitope inserted into the scaffold of GFP proved beneficial in enhancing the detection of Piezo2 in the skin beyond what was possible with a published Piezo2 reporter line<sup>26,36</sup> and appeared to have no effect on general ambulatory behavior in homozygous transgenic animals, suggesting conserved function of the Piezo2 channel (Figures S1D and S1E). When hairy and glabrous skin of *Piezo2*<sup>smFP-FLAG</sup> mice were co-stained with anti-FLAG and anti-neurofilament heavy chain (NFH, a reporter for A $\beta$  axons), we observed spatial colocalization of Piezo2-FLAG and NFH in A $\beta$  sensory axons forming lanceolate and circumferential endings around hair follicles and along the A $\beta$  sensory axons innervating the Meissner corpuscles in glabrous skin and Pacinian corpuscles associated with bones (Figures 1B, S1F, and S1G). While Piezo2 was localized to the terminal portion of A $\beta$  axons forming the end organ structures, it was noticeably absent from NFH<sup>+</sup> axon fibers before they entered the end organ structures (Figure 1B). Piezo2 was also absent from resident non-myelinating Schwann cells, most easily appreciated by the lack of Piezo2-FLAG labeling in the S100<sup>+</sup> and PLP<sup>EGFP+</sup> lamellar cells within the Meissner and Pacinian corpuscles, respectively (Figure S1F). Strikingly, we found small, Piezo2<sup>+</sup>, spine-like protrusions (~1  $\mu$ m in length) that emanated from the NFH<sup>+</sup> axons (Figure S1F) forming the

of the fibula. Diagrams illustrate end organs with A $\beta$  RA-LTMRs in magenta. Representative confocal images show A $\beta$  RA-LTMRs (NFH<sup>+</sup>) and specialized non-neuronal Schwann cells (S100B<sup>+</sup>) of each end organ. Dashed lines outline the hair follicle (left), dermal papilla (middle), and boundary of outer and inner core (right). Scale bar, 20  $\mu$ m.

(B) Top: schematic diagram of the *Piezo2*<sup>smFP-FLAG</sup> allele. Bottom: confocal images of Piezo2-FLAG localization to A $\beta$  RA-LTMR axons (NFH<sup>+</sup>) in the three end organs. Red arrowheads indicate co-localized FLAG and NFH signal. Blue arrowheads indicate axonal NFH signal outside the end organ that lacks FLAG signal. This experiment was repeated in two animals with littermate controls. Scale bar, 25  $\mu$ m.

(C) Immuno-electron micrographs from a *Piezo2*<sup>smFP-FLAG</sup> animal stained for FLAG with silver enhancement show localization of the Piezo2-FLAG fusion protein along the membranes of A $\beta$  RA-LTMRs (pseudo-colored pink). Pink arrowheads indicate a subset of Piezo2-FLAG puncta along sensory axon membranes; green arrowheads indicate a subset of puncta along axon protrusions. Piezo2-FLAG is also localized to the membrane of A $\beta$  field-LTMR circumferential endings around the guard hair (blue). This experiment was repeated in two animals with littermate controls. Scale bar, 1  $\mu$ m.

(D) Same as in (C) but for wild-type littermate of the *Piezo2*<sup>smFP-FLAG</sup> animal.

See also Figures S1 and S2.



lanceolate endings, Meissner corpuscles, and Pacinian corpuscles, hinting at the presence of a conserved ultrastructural feature of A $\beta$  RA-LTMRs that may be involved in mechanotransduction.

Within each mechanosensory end organ, A $\beta$  RA-LTMR axons associate with non-myelinating Schwann cells, referred to as terminal Schwann cells (TSCs) in hairy skin and lamellar cells in Meissner corpuscles and Pacinian corpuscles. Whether TSCs and lamellar cells serve as passive modulators of mechanical forces impinging on the sensory axon or play an active role in initiating mechanical responses is an area of active investigation.<sup>41–43</sup> Deleting *Piezo2* in both somatosensory neurons and non-neuronal cells leads to complete loss of light-touch responses measured in the DRG, spinal cord, and brainstem, emphasizing the critical role of *Piezo2* in light touch.<sup>29,30</sup> However, definitively answering whether *Piezo2* is expressed and functions within the axon terminals or non-neuronal cells requires a high-resolution *Piezo2* localization approach and physiological analyses of mice lacking *Piezo2* only in non-neuronal cells. Therefore, we next performed immunoelectron microscopy (immuno-EM) with samples from *Piezo2*<sup>smFP-FLAG</sup> animals to determine the cell-type-specific and subcellular localization of *Piezo2* within the end organs. We observed *Piezo2*-FLAG enriched along the sensory axon membranes in all three end organs (Figures 1C and S2A), consistent with our light microscopy findings. *Piezo2*-FLAG was localized to A $\beta$  RA-LTMR membranes of hair follicle lanceolate endings, A $\beta$  field-LTMR circumferential endings surrounding hair follicles, and A $\beta$  LTMR terminals in Meissner corpuscles and Pacinian corpuscles (Figures 1C and S2A). Similar to the *Piezo2*<sup>+</sup> spine-like processes observed by light microscopy, we also observed *Piezo2*-FLAG localization along small protrusions that extend beyond the main body of the A $\beta$  LTMR axons (Figures 1C and S2A), suggesting that these curious finger-like structures—first described over 50 years ago<sup>23,44–47</sup>—may participate in mechanical gating of the channel. Subcellular quantification of puncta density and size across end organs revealed that unlike the select enrichment of *Piezo2* puncta along the sensory axon membrane of *Piezo2*-FLAG animals, little, if any, immunostaining signal localized to the membranes of TSCs and lamellar cells above the level of background staining observed in non-transgenic controls (Figures 1C, 1D, and S2A–S2D). Consistent with this observation, electrophysiological recordings in *Dhh-Cre; Piezo2*<sup>fl/fl</sup> mice showed that deleting *Piezo2* in TSCs and lamellar cells, but not in neurons, did not affect mechanosensitivity or response properties of A $\beta$  mechanosensory neurons (Figures 2A–2E). This is in contrast to the near-complete loss of low-threshold responses in *Cdx2-Cre; Piezo2*<sup>fl/fl</sup> mice, which lack *Piezo2* in both somatosensory neurons and non-neuronal cells (Figure 2B). This dramatic difference in tactile sensitivity is mirrored at the behavioral level, where deletion of *Piezo2* in *Dhh*<sup>+</sup> Schwann cells has little effect on general ambulatory behavior while deletion of *Piezo2* in sensory neurons leads to severe motor deficits (Figures S3A and S3B). Taken together, our light microscopy, immuno-EM, and genetic manipulations and electrophysiological findings indicate that in all three end organs the A $\beta$  RA-LTMR sensory axon serves as the main site of *Piezo2*-dependent mechanotransduction, consistent with previously published data.<sup>26,27,48,49</sup>

### FIB-SEM volumes of three A $\beta$ RA-LTMR end organs

Key insights into mechanotransduction in the cochlea were revealed by classical 3D scanning electron microscopy (SEM) analysis of cochlear hair cells. This 3D analysis led to the discovery of hair cell stereocilia tip links that bridge stereocilia and the widely accepted model for how mechanical forces generated by stereocilia movement are transduced into channel gating and hair cell depolarization.<sup>50–52</sup> In an attempt to gain a comparable level of insight for tactile sensory neurons, we visualized the 3D architecture of the three A $\beta$  RA-LTMR end organs in their native tissue context to identify ultrastructural features that may underlie mechanotransduction across these morphologically dissimilar A $\beta$  LTMR end organs. For this, we applied enhanced focused ion beam SEM (FIB-SEM)<sup>53</sup> to image the three end organs in their entirety with 6-nm isotropic voxels (Figures 3A–3D). Coupled with deep-learning-based segmentation,<sup>54</sup> we reconstructed the A $\beta$  RA-LTMR axons of a guard hair lanceolate complex, two Meissner corpuscles, and a Pacinian corpuscle to generate high-resolution 3D renderings of these A $\beta$  RA-LTMR end organs.

### 3D architecture of the guard hair lanceolate complex

In hairy skin, we imaged a  $5.12 \times 10^5 \mu\text{m}^3$  volume of tissue containing the entire A $\beta$  RA-LTMR lanceolate complex surrounding a guard hair follicle, which is the longest hair type on the mouse trunk and accounts for 1% of all trunk hair follicles (Figure 3A). We identified and reconstructed all 47 lanceolate endings formed by heavily myelinated A $\beta$  axons that encircle the outer root sheath of the hair follicle (Figure 4A; Video S1). We presume these to be the endings of two or three A $\beta$  RA-LTMR neurons based on prior anatomy studies.<sup>8,55</sup> All but one axon branched at the base of the hair follicle complex to form multiple interdigitated lanceolate endings that extend within the longitudinal collagen matrix along the length of the hair shaft. In addition to the 47 A $\beta$  RA-LTMR lanceolate endings, we were surprised to find six lanceolate endings formed by four unmyelinated, small-caliber axons (Figure S4A). Smaller-diameter A $\delta$ - and C-LTMRs also form lanceolate endings associated with awl/auchene and zigzag hair follicles, but not guard hair follicles<sup>8</sup>; however, calcitonin gene-related peptide (CGRP) antibody staining in hairy skin revealed CGRP<sup>+</sup>, NFH<sup>+</sup> lanceolate endings (Figure S4B), suggesting that small-diameter CGRP<sup>+</sup> fibers may form a small subset of lanceolate endings surrounding hair follicles. Each lanceolate ending was associated with processes originating from one to three of the 17 TSCs, which were also embedded within the longitudinal collagen matrix and were fully reconstructed. These 17 TSCs were mostly non-overlapping, tiling the hair follicle, and had cell bodies located at the base of the lanceolate complex (Figure 4D; Videos S2 and S3), consistent with a previous report.<sup>21</sup> Although the TSC processes formed an overlay that covered the lanceolate axons along their full extension adjacent to the hair shaft, intermittent gaps in TSC coverage formed at the boundaries of TSC processes, leaving exposed small portions of axon membrane along the full length of the lanceolate complex. These gaps most often formed on opposite sides of the lanceolate ending, along the axon membrane proximal and distal to the outer root sheath (Figures 4A and S4C). The membranes of TSCs were studded with membrane pits that appeared structurally analogous to lipid-raft

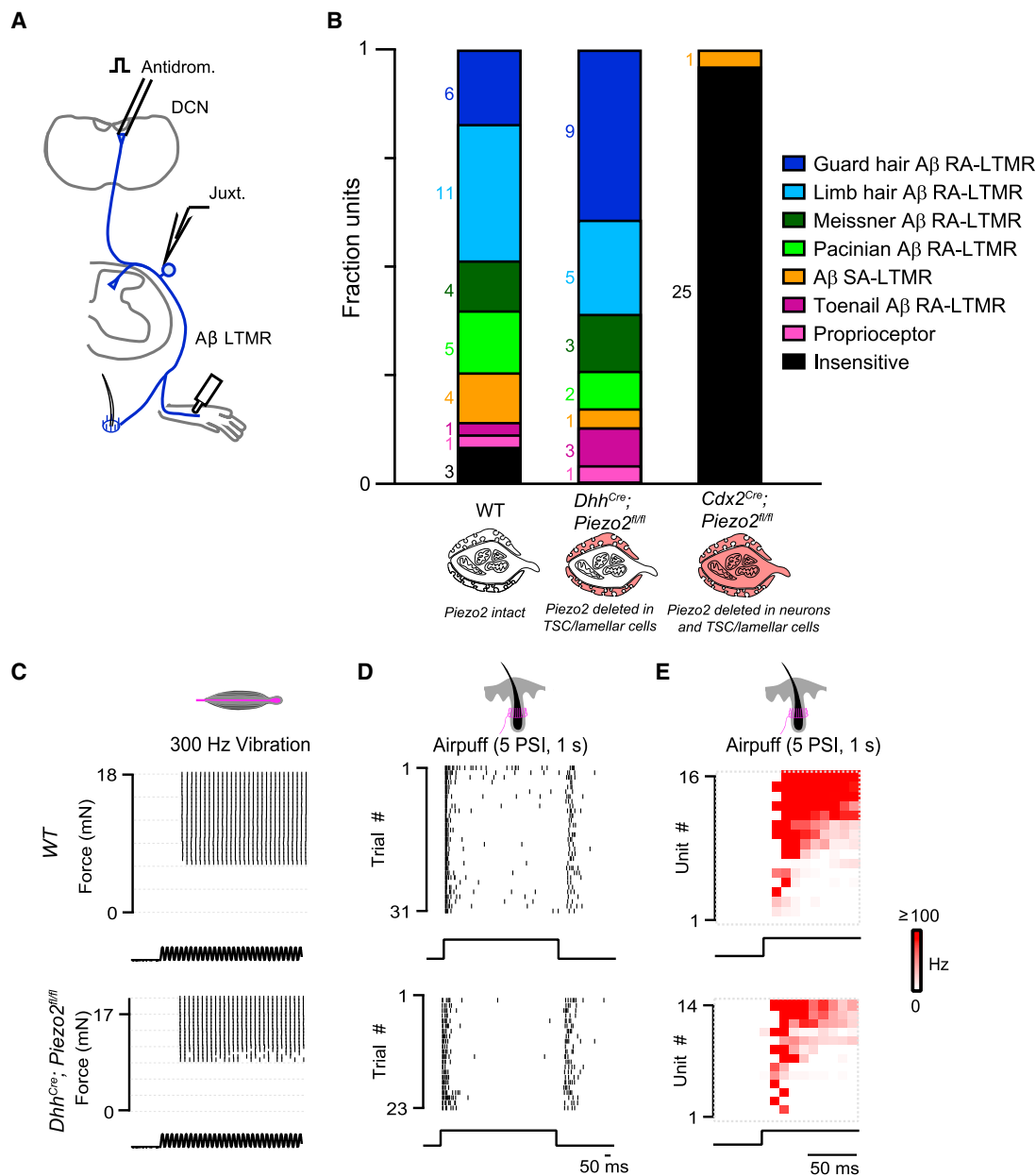


**Figure 2. Deletion of Piezo2 in TSCs and lamellar cells does not affect light-touch responses in Aβ sensory neurons**

(A) Schematic of juxtacellular recordings. Aβ sensory neurons were identified with antidromic activation of the dorsal column nucleus (DCN) or dorsal column (DC). Mechanical stimuli were applied to the hindpaw and hairy thigh.

(B) The fraction of DCN-projecting units identified as a specific sensory neuron class based on the location of receptive field and response to low-threshold mechanical stimuli in wild-type (WT) animals (n = 3), *Dhh<sup>Cre</sup>; Piezo2<sup>fl/fl</sup>* mice (n = 3), and *Cdx2<sup>Cre</sup>; Piezo2<sup>fl/fl</sup>* mice (n = 2).

(C) Raster of single Pacinian Aβ RA-LTMR responses to vibration (300 Hz) at different forces in a WT (top) and a *Dhh<sup>Cre</sup>; Piezo2<sup>fl/fl</sup>* (bottom) animal.

(D) Same as in (C) but for hairy skin Aβ RA-LTMR responses to air puff.

(E) Histograms of air puff responses for all Aβ hairy units activated by DCN stimulation in WT (top) and *Dhh<sup>Cre</sup>; Piezo2<sup>fl/fl</sup>* (bottom) animals. In WT animals, 15/16 hairy units tested with air puff were air-puff sensitive. In the *Dhh<sup>Cre</sup>; Piezo2<sup>fl/fl</sup>* animals, 13/14 hairy units tested with air puff were air-puff sensitive.

See also Figure S3.

structures called caveolae, which are found in several cell types, including skeletal and endothelial cells.<sup>56</sup> Indeed, deletion of the *Caveolin1* gene led to loss of these structures within TSCs of hairy skin (Figures S4C and S4D).

Distal to the outer root sheath and longitudinal collagen network lies the circumferential collagen matrix that encircles the hair shaft at an orientation perpendicular to the longitudinal collagen network and contains the circumferential endings of

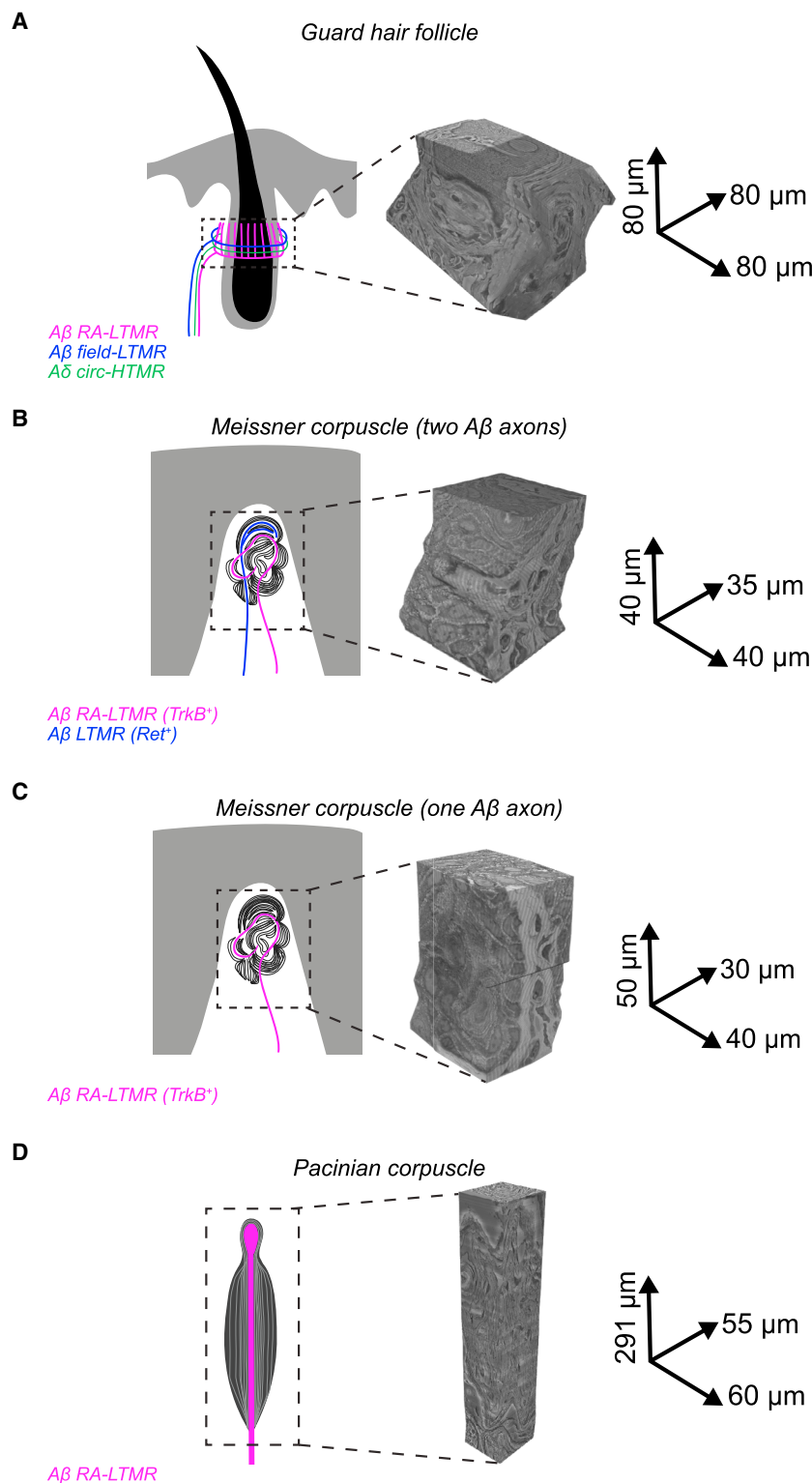


**Figure 3. Aligned FIB-SEM volumes of end organs formed by A $\beta$  RA-LTMRs**

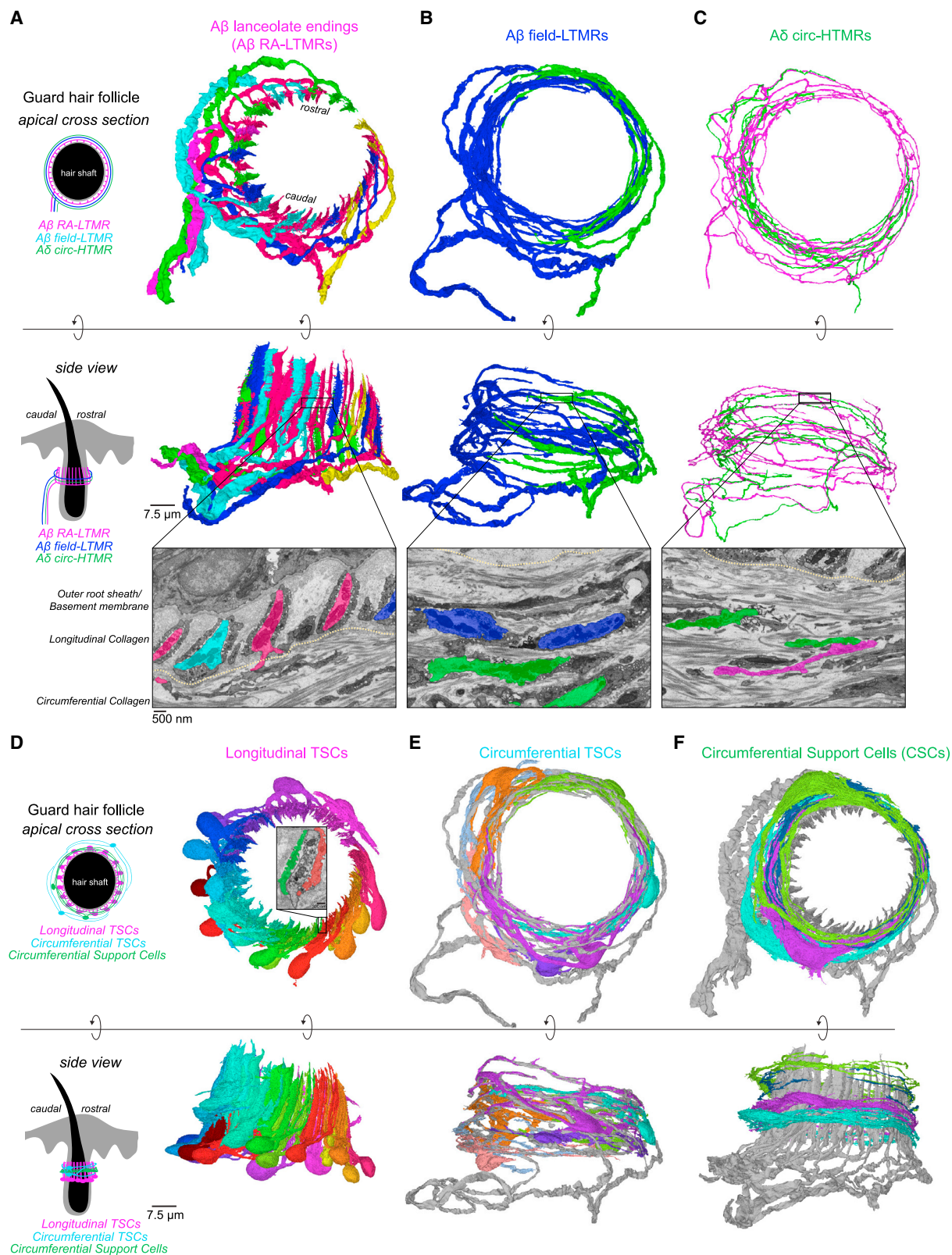
FIB-SEM volumes with global alignment correction and dimensions for skin samples containing (A) a single guard hair, (B) a Meissner corpuscle with two myelinated afferents, (C) a Meissner corpuscle with a single myelinated afferent, and (D) a Pacinian corpuscle.

late endings but also in their mechanical tuning properties. While A $\beta$  field-LTMRs are sensitive to gentle stroking across the skin, both circumferential-ending neuron types exhibit a higher activation threshold in response to skin indentation when compared to A $\beta$  RA-LTMRs.<sup>2,57,59</sup> Within the volume, we identified and reconstructed two large-caliber, myelinated axons we presume to be A $\beta$  field-LTMRs, and we reconstructed a subset of circumferential TSCs that associated with these large-caliber axons (Figures 4B and 4E; Video S4). We also reconstructed two small-diameter axons within the circumferential collagen matrix that have morphological properties of circumferential CGRP<sup>+</sup> A $\delta$  circ-HTMR endings (Figures 4C and S4E; Video S5). The designation of A $\beta$  field-LTMRs and CGRP<sup>+</sup> A $\delta$  circ-HTMRs in our volume was further validated in parallel by genetically labeling each subtype with an EM reporter<sup>60</sup> and identifying ultrastructural homology by single-section transmission electron microscopy (TEM) (Figure S4F). Indeed, by TEM, we observed abundant neurofilaments in A $\beta$  field-LTMRs that were noticeably absent from small-diameter CGRP<sup>+</sup> A $\delta$  circ-HTMRs, an ultrastructural distinction also observed between the two classes of circumferential endings in our FIB-SEM volume. In addition to the sensory axons and TSCs within the circumferential collagen, we found an extensive network of ~17 non-neuronal cells, which we term circumferential support cells (CSCs). These previously uncharacterized CSCs were structurally distinct from TSCs in their minimal association with circumferential sensory axons. We reconstructed a subset of CSCs whose cell bodies reside in the circumferential collagen network distal to the lanceolate complexes and found that they fully

the A $\beta$  field-LTMRs and CGRP<sup>+</sup> A $\delta$  circumferential high-threshold mechanoreceptors (A $\delta$  circ-HTMRs).<sup>2,57,58</sup> These two circumferential sensory neurons are distinct from A $\beta$  RA-LTMRs not just in their perpendicular orientation to the lanceo-

encircle the guard hair in a vertically tiled manner (Figure 4F; Video S6).

To identify structural features underlying the heightened sensitivity of A $\beta$  RA-LTMRs to mechanical forces, we examined



(legend on next page)



features unique to the A $\beta$  RA-LTMR lanceolate complexes. One strikingly unique ultrastructural feature of the A $\beta$  RA-LTMRs was the presence of numerous axon protrusions that emerged only where the sensory axon formed close associations with TSCs (Figures 5A–5C), a location coincident with the axolemmal expression of Piezo2 (Figures 1B and S1F). These axon protrusions appeared along the length of lanceolate endings at a density of 1.9 protrusions/ $\mu$ m of axon and extended through the intermittent gaps between TSC processes (Figures 5B and 5C). Moreover, protrusions were absent from the TSC gaps proximal to the outer root sheath epithelial cells (Figure 5C) and were sparse or lacking in both the six small-caliber lanceolate endings and the circumferential endings of A $\beta$  field-LTMRs and CGRP $^{+}$  A $\delta$  circ-HTMRs (Figures S4A and S5A). Of the 1,742 axon protrusions originating from the 47 A $\beta$  RA-LTMR lanceolate endings, 51% (880/1,742) reached beyond the local longitudinal collagen matrix and extended into the circumferential collagen network (Figures 5D and S5B). Because of the potential for unique biomechanical properties at the longitudinal/circumferential collagen matrix interface during mechanical stress, we examined the properties of the axon protrusions that extended across the interface and into the circumferential collagen region. We found that 57.3% (504/880) of these axon protrusions formed close associations with resident cells of the circumferential collagen matrix (Figures 5D, 5E, and S5B). Furthermore, a significant proportion (32%, 163/504) of these contacts formed with the four reconstructed CSCs (Figure 5E; Video S7). In contrast, only a single contact was observed between the axon protrusions and the seven reconstructed circumferential TSCs (Figure S5C), revealing a preferential association between the axon protrusions and CSCs. These findings suggest that an extensive series of contacts between A $\beta$  RA-LTMR lanceolate axon protrusions and CSCs serve to bridge the A $\beta$  lanceolate endings across two perpendicularly oriented collagen matrices and anchor the sensory axon within the circumferential collagen region. We also observed lanceolate ending axon protrusions that contact non-neuronal cells within the circumferential collagen network of non-guard hairs, most of which are innervated exclusively by A $\delta$ -LTMRs and C-LTMRs (Figure S5D). This ultrastructural motif conserved across LTMRs that form lanceolate endings around hair follicles suggests a model in which hair deflection or local skin indentation moves the circumferential collagen matrix relative to the longitudinal collagen matrix, thereby stretching axon protrusions and gating Piezo2 localized within the axon membrane of lanceolate endings.

### 3D architecture of the Meissner corpuscle

We next sought to determine whether similar ultrastructural features were prevalent in other A $\beta$  RA-LTMR end organs and, if so,

whether a common model may explain mechanotransduction across them. Therefore, we imaged a  $5.6 \times 10^4 \mu\text{m}^3$  volume of glabrous skin containing a Meissner corpuscle innervated by two myelinated A $\beta$  LTMRs (Figures 3B and 6A; Video S8). We reconstructed these two A $\beta$  LTMRs innervating the Meissner corpuscle, in addition to their associated lamellar cells and a subset of unmyelinated axons associated with the corpuscle, which may correspond to peptidergic and non-peptidergic C-fibers (Figures 6A–6C and S6A).<sup>61</sup> By confocal microscopy, the Meissner corpuscle appears as a spherical end organ with tortuous NFH $^{+}$  axons (Figure 1A). However, our reconstruction revealed two A $\beta$  LTMR axons that traveled through the corpuscle in a largely linear manner (Figures 6A and 6B), remarkably analogous in appearance to the hair follicle-associated A $\beta$  RA-LTMR lanceolate endings (Figure 5A). While the central Meissner A $\beta$  axon was unbranched and shed its myelin at the base of the corpuscle structure, the more apical A $\beta$  axon branched earlier within the dermal papilla and continued unmyelinated for 27.4  $\mu$ m before entering the corpuscle (Figure 6A). Four lamellar cells with cell bodies situated at the edge of the corpuscle extended numerous interdigitated lamellar processes to form the characteristic multi-layered wrappings of Meissner A $\beta$  LTMRs (Figure 6C). Three of the four lamellar cells contributed to the innermost wrapping of both A $\beta$  LTMR axons, revealing a high degree of interconnectedness of axons and lamellar cells within this structure (Figure 6C). As with the TSCs of hairy skin, caveolae appeared along the lamellar cell membrane; these were absent in mice lacking the *Caveolin1* gene (Figure S6B), revealing a conserved structural feature of TSCs of hair follicles and lamellar cells of Meissner corpuscles. Moreover, as with hair follicle TSCs, the corpuscle's lamellar cells had intermittent gaps in coverage along the sensory axon body (Figures 6C and S6C). These gaps often appeared at the vertices of the ellipsoid axon profile and their position remained consistent across the corpuscle. Strikingly similar to what we observed for hair follicle A $\beta$  RA-LTMR lanceolate endings, an extensive array of axon protrusions emerged between these gaps and extended into the surrounding collagen network (Figure 6C). These protrusions were restricted to the portion of axon within the corpuscle proper, suggestive of a role in mechanotransduction given their proximity to membrane-bound Piezo2 (Figures 1C, 6A–6C, S1F, and S2A).

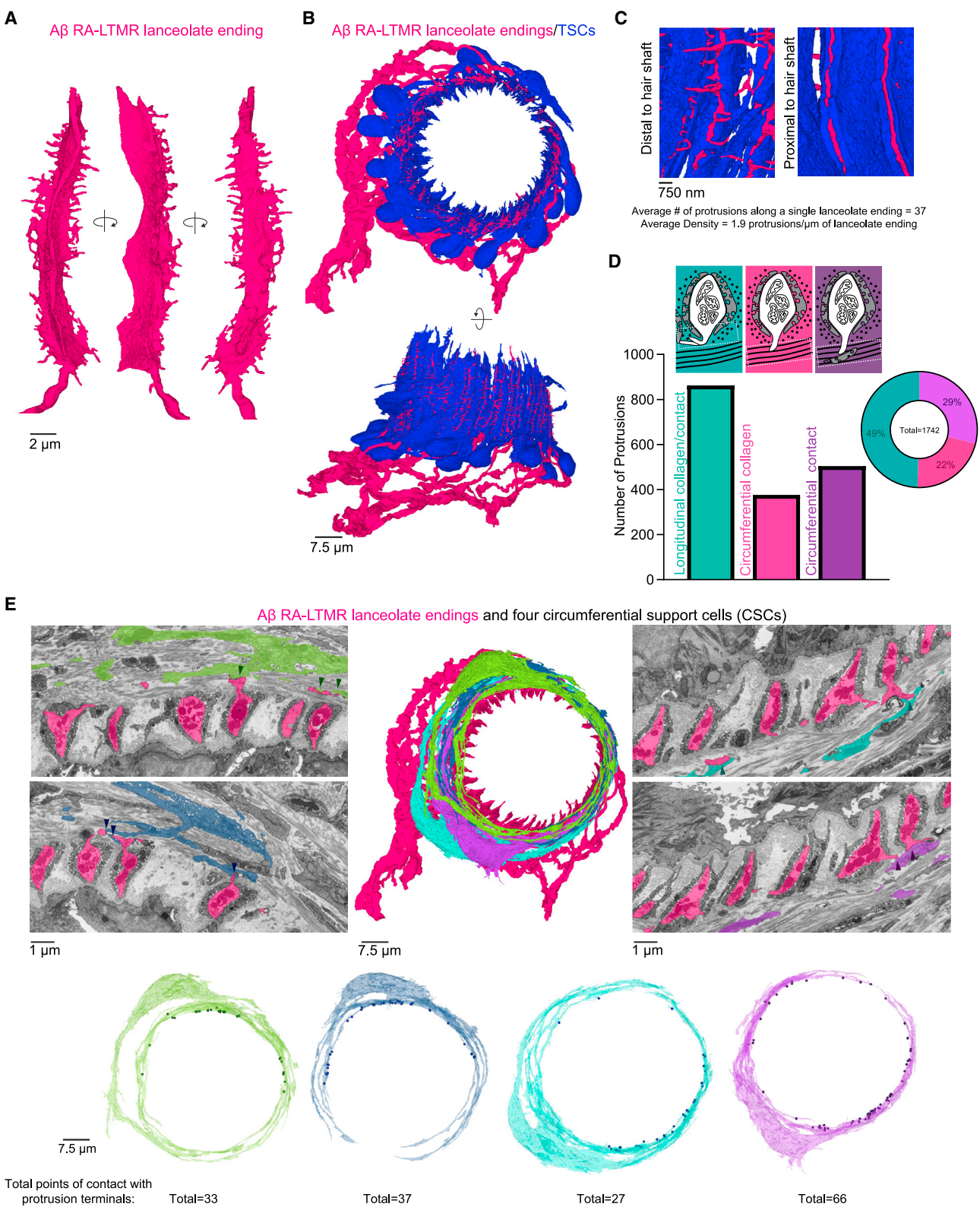
Within most Meissner corpuscles exist two molecularly and physiologically distinct A $\beta$  LTMRs.<sup>3</sup> The TrkB $^{+}$  Meissner afferent is the stereotypical, highly sensitive A $\beta$  RA-LTMR, while the Ret $^{+}$  Meissner afferent is, on average, less sensitive to skin indentation and exhibits varying rates of adaptation.<sup>3</sup> In addition to being molecularly and physiologically distinct, these two neuronal populations have distinct interactions with lamellar cells. Previous

### Figure 4. FIB-SEM reconstructions of A $\beta$ and A $\delta$ sensory neuron endings and associated non-neuronal cells of a guard hair follicle

(A–C) 3D renderings of sensory neurons innervating a mouse guard hair follicle shown from an apical view (top) and from a side view (middle). Bottom: pseudo-colored images from the FIB-SEM volume with the boundary between longitudinal and circumferential collagen matrix marked by the yellow line. (A) Six A $\beta$  RA-LTMR axon segments form 47 lanceolate endings, (B) two A $\beta$  field-LTMRs, and (C) two A $\delta$  circ-HTMRs form circumferential endings.

(D–F) 3D renderings of (D) 17 TSCs within the longitudinal collagen that form intimate associations with lanceolate endings. Inset: an example of two different TSCs associated with the same lanceolate ending; (E) seven circumferential TSCs within the circumferential collagen matrix that associate with A $\beta$  field-LTMRs (gray); (F) four CSCs within the circumferential collagen matrix that frequently contact axon protrusions of A $\beta$  RA-LTMR lanceolate endings (gray).

See also Figure S4.



(legend on next page)

work detailing ultrastructural distinctions across the two Meissner afferent subtypes found that lamellar cell processes associated with the axons of TrkB<sup>+</sup> A $\beta$  RA-LTMRs were more elaborate and numerous than those associated with Ret<sup>+</sup> A $\beta$  LTMRs.<sup>3</sup> In our 3D reconstruction, we found that across all depths of the corpuscle, the central axon (Figures 6C and S6E, magenta) was wrapped more extensively by lamellar cell processes, suggestive of the central axon being TrkB<sup>+</sup> and the peripheral axon being Ret<sup>+</sup>.

Using this classification for the two axons, we analyzed the axon protrusion density across these two subtypes. We found that the putative TrkB<sup>+</sup> A $\beta$  RA-LTMR axon formed more than twice as many axon protrusions as the putative Ret<sup>+</sup> axon (396 and 162, respectively) and had 11.7 protrusions/ $\mu$ m of axon—a density roughly four times that of the putative Ret<sup>+</sup> axon (3.0 protrusions/ $\mu$ m), revealing a second ultrastructural distinction for these two subtypes that may underlie their difference in tactile sensitivity (Figure 6D). To test whether the density of axon protrusions along TrkB<sup>+</sup> axons was consistent across corpuscles, we reconstructed the A $\beta$  axon of a second, singly innervated Meissner corpuscle from a different FIB-SEM volume (Figures 3C and S6D). As at least 80% of corpuscles within the forepaw digits receive a TrkB<sup>+</sup> afferent (Figure S6F), and because Meissner corpuscles are virtually absent in sensory neuron-specific TrkB knockout mice,<sup>3</sup> we presumed that the axon of this singly innervated Meissner corpuscle was TrkB<sup>+</sup>. We found that the presumed TrkB<sup>+</sup> afferent of the singly innervated Meissner corpuscle was centrally located in the corpuscle and wrapped by numerous lamellar cell processes—features paralleled by the TrkB<sup>+</sup> axon of the dual-innervated Meissner corpuscle (Figures S6D and S6E). Moreover, the axon of the singly innervated Meissner corpuscle had a density of 15.1 protrusions/ $\mu$ m of axon, a value comparable to the TrkB<sup>+</sup> axon of the dual-innervated Meissner (Figure 6D). Importantly, in characterizing the terminal structure of the axon protrusions from both corpuscles, we observed a conserved structural motif analogous to A $\beta$  RA-LTMR hair follicle lanceolate endings. We found that 62% (334/538) and 67% (264/396) of protrusions from the presumed TrkB<sup>+</sup> axon of the single- and dual-innervated Meissner corpuscles, respectively, contacted lamellar cell processes within the corpuscle (Figure 6D; Video S9). Although the density of protrusions was lower in the presumed Ret<sup>+</sup> axon of the dual-innervated Meissner corpuscle, a similar proportion of its protrusions formed intimate associations with lamellar cells (60%, 97/162) (Figure 6D). The heightened density of axon protrusions in the more mechanically sensitive TrkB<sup>+</sup> A $\beta$  RA-LTMRs, compared to the Ret<sup>+</sup> A $\beta$  LTMR, suggests that these structures and their

contacts throughout the end organ structure may contribute to the high sensitivity and low-activation threshold of TrkB<sup>+</sup> A $\beta$  RA-LTMR axons of Meissner corpuscles in a manner analogous to the lanceolate endings of hair follicles.

### 3D architecture of the Pacinian corpuscle

The third end organ structure innervated by A $\beta$  RA-LTMRs, the Pacinian corpuscle, is altogether unique in its size, location, simplicity in morphological appearance, and sensitivity to high-frequency vibrations. Pacinian corpuscles of the mouse are mostly restricted to the periosteum surrounding bones and are 200–300  $\mu$ m in length and  $\sim$ 40  $\mu$ m in diameter (Figure 1A).<sup>62,63</sup> Each Pacinian corpuscle is innervated by a single A $\beta$  RA-LTMR axon that extends the length of the corpuscle, typically unbranched, before terminating in a branched, bulbous structure called the ultraterminal region.<sup>63</sup> Encircling the central axon are numerous concentric cellular processes formed by non-neuronal cells.<sup>46</sup> The innermost rings that form the inner core around the axon are established by lamellar cells analogous to those of the Meissner corpuscle.<sup>64</sup> Although the A $\beta$  LTMR of the Pacinian is analogous to the A $\beta$  lanceolate ending and Meissner afferents in its RA response to static indentation, it is unique in its sensitivity to high-frequency vibrations (>200 Hz).<sup>15,16</sup> To visualize the 3D ultrastructural features of the Pacinian A $\beta$  RA-LTMR, we imaged a  $9.6 \times 10^5 \mu\text{m}^3$  volume of tissue isolated from the periosteum membrane surrounding the fibula of a mouse and containing a Pacinian corpuscle (Figure 3D). We identified and reconstructed a single A $\beta$  RA-LTMR axon that shed its myelin upon entering the corpuscle and remained unbranched within the terminal region for  $\sim$ 200  $\mu$ m before branching and entering the ultraterminal region (Figure 7A; Video S10). Within the terminal region, the cellular architecture remained simple and consistent. There, the A $\beta$  RA-LTMR axon was ellipsoid (1.5  $\mu$ m  $\times$  4.5  $\mu$ m) with its major axis aligned with the longitudinal cleft (Figure 7B), whose orientation was maintained throughout the terminal region. The multi-layered wrapping of the inner core region was established by  $\sim$ 73 lamellar cells whose cell bodies were situated at the inner/outer core boundary (Figure S7A). The thin and densely packed lamellar cell processes emerging from the 73 lamellar cells precluded their complete reconstruction; however, we used ROSA26-Confetti, a stochastic, multicolor Cre-dependent fluorescent mouse reporter line, with a *Plp1-CreER* mouse to reveal the intermingled nature of lamellar cell processes within the Pacinian corpuscle (Figure S7B). Furthermore, we reconstructed a subset of lamellar processes originating from two distinct lamellar cells over a small portion of the terminal region within the FIB-SEM volume. Within

**Figure 5. Axon protrusions along A $\beta$  RA-LTMRs extend through TSC openings and contact CSCs within the guard hair's circumferential collagen network**

- (A) A single lanceolate ending with numerous axon protrusions shown from multiple perspectives.  
 (B) Apical and side views of A $\beta$  RA-LTMRs (magenta) and associated TSCs (blue).  
 (C) Axon protrusions emerge at TSC gaps distal to the hair shaft.  
 (D) Quantification of axon protrusion terminals. Teal, protrusions that terminate in local longitudinal collagen with or without making contact with local TSCs; magenta, protrusions that extend into circumferential collagen but do not form cell contacts; purple, protrusions that extend into circumferential collagen and form cell contacts.  
 (E) Axon protrusions of A $\beta$  RA-LTMRs that extend into the circumferential collagen network frequently contact four reconstructed CSCs (arrowheads). Points where each CSC contacts an axon protrusion are marked as dots on the 3D rendering of the cell.  
 See also Figure S5.



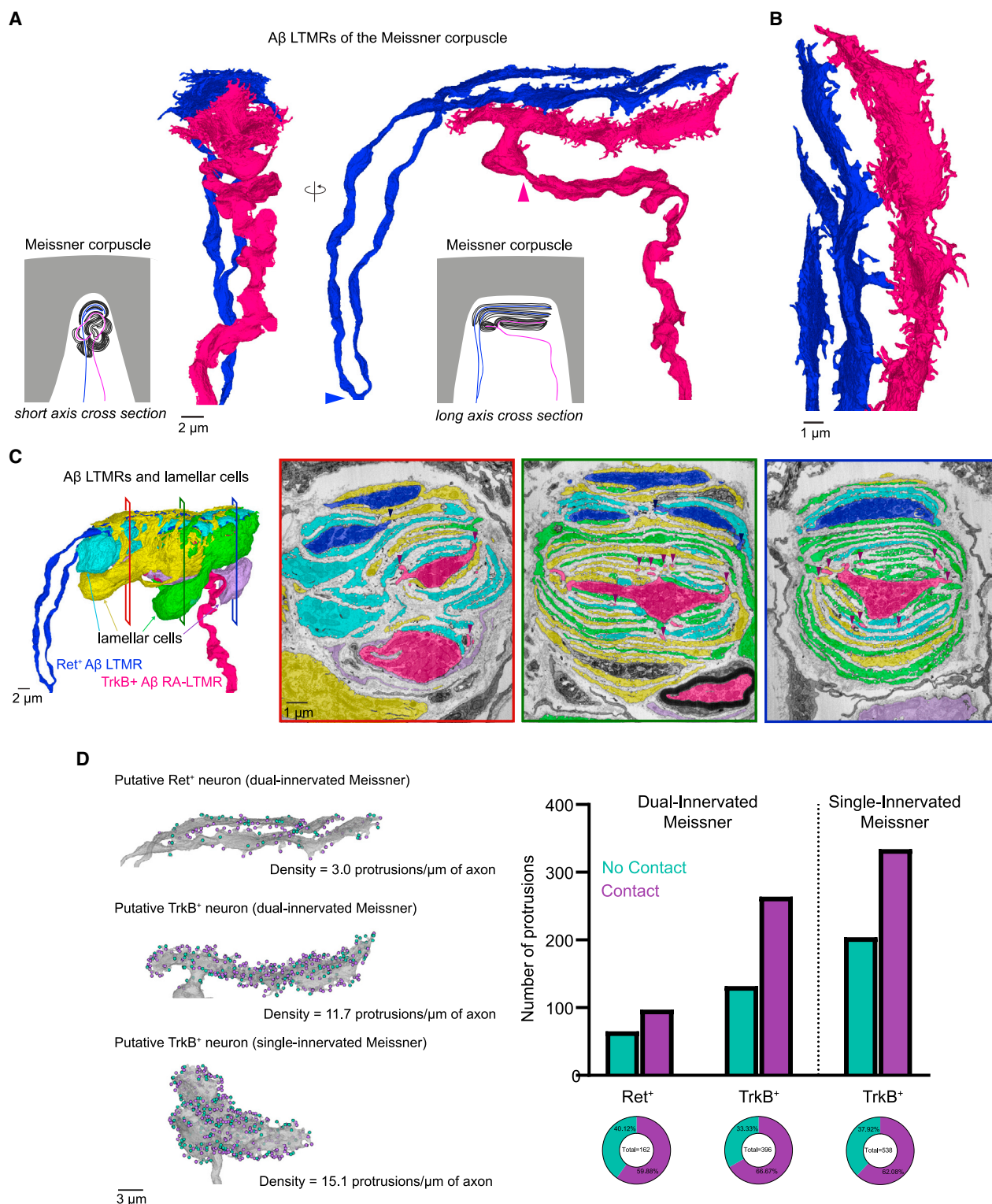


**Figure 6. FIB-SEM reconstructions of two Meissner corpuscles reveal the density of axon protrusions to be a structural correlate of A $\beta$  LTMR tactile sensitivity**

(A) 3D renderings of two A $\beta$  LTMRs that innervate a Meissner corpuscle. Arrowheads indicate the termination of myelination.

(B) Higher-magnification rendering of the terminal portion of the two A $\beta$  LTMRs.

(legend continued on next page)



this 5  $\mu\text{m}$  portion of the terminal region, we observed a handful of processes that emerged from the two lamellar cell bodies and established intermingled layers spanning the inner core region (Figure S7C). Together, these results reveal a blending of lamellar cell processes analogous to that observed within the Meissner corpuscle (Figure 6C). Intermittent gaps in lamellar cell coverage formed along the axon at the vertices of the major axis, leaving the portion of axon membrane closest to the two longitudinal clefts exposed. As with the A $\beta$  RA-LTMRs in hairy and glabrous skin, an extensive array of axon protrusions emerged from the central axon at these gaps and extended into the collagen matrix of the cleft (Figure 7B). The structure of these axon protrusions was more complex than the A $\beta$  RA-LTMRs of the hair follicle or Meissner corpuscle, resembling a tree with a trunk-like base from which numerous protrusions extended like branches. The base of these protrusions was often structurally supported by a dense, local collagen network that encircled the structure and disintegrated as the protrusions extended from the central axon and branched (Figure S7D). Because of the large size of the corpuscle and the density of protrusions within it, we characterized the protrusion density and terminal structure across four small regions of the volume and used these measurements to estimate the total number of protrusions across the corpuscle. We estimate that there are  $\sim 3,124$  protrusions within the terminal region occurring at a density of 18.6 protrusions/ $\mu\text{m}$  of axon. We also estimate that  $\sim 57.9\%$  (1,809/3,124) of these protrusions terminated by contacting lamellar cell processes in the inner core (Figure 7D), revealing a conserved structural motif analogous to the A $\beta$  RA-LTMR lanceolate ending and Meissner corpuscle.

As the Pacinian's A $\beta$  RA-LTMR axon transitioned from the terminal to ultraterminal region, it branched and its structure became far more complicated. Within the  $\sim 60\text{-}\mu\text{m}$ -long ultraterminal region, which included 123  $\mu\text{m}$  of axon, the axon expanded up to 12  $\mu\text{m}$  in diameter and contained a remarkably high density of mitochondria (Figure 7C). Accompanying the dissolution of the lamellar cell cleft was the emergence of axon protrusions of greater prevalence and structural complexity at many points along the circumference of the axon. The density of axon protrusions in the Pacinian's ultraterminal region was estimated to be twice that of the terminal region, with 36.4 protrusions/ $\mu\text{m}$  of axon (estimated total = 4,470 protrusions). Across the two sampled regions of axon within the ultraterminal region, we found that 52.3% of protrusions terminated by contacting lamellar cell processes, suggesting that  $\sim 2,339$  protrusions within the ultraterminal region likely form intimate contacts with lamellar cells (Figure 7D; Video S11). Some of the terminals of the longer and more elaborate protrusions were encased by cells at the edge of the inner core or extended beyond the inner core to contact the innermost edge of the cells forming the outer core (Figure 7C). The dense arrangement of axon protrusions within the ultraterminal region and their complex structure and reach

across the inner and outer core boundary may impart elastic properties to the axon that facilitate its sensitivity to high-frequency pressure transients and vibration across the entire corpuscle structure.

### Comparison of axon protrusions across end organ structures

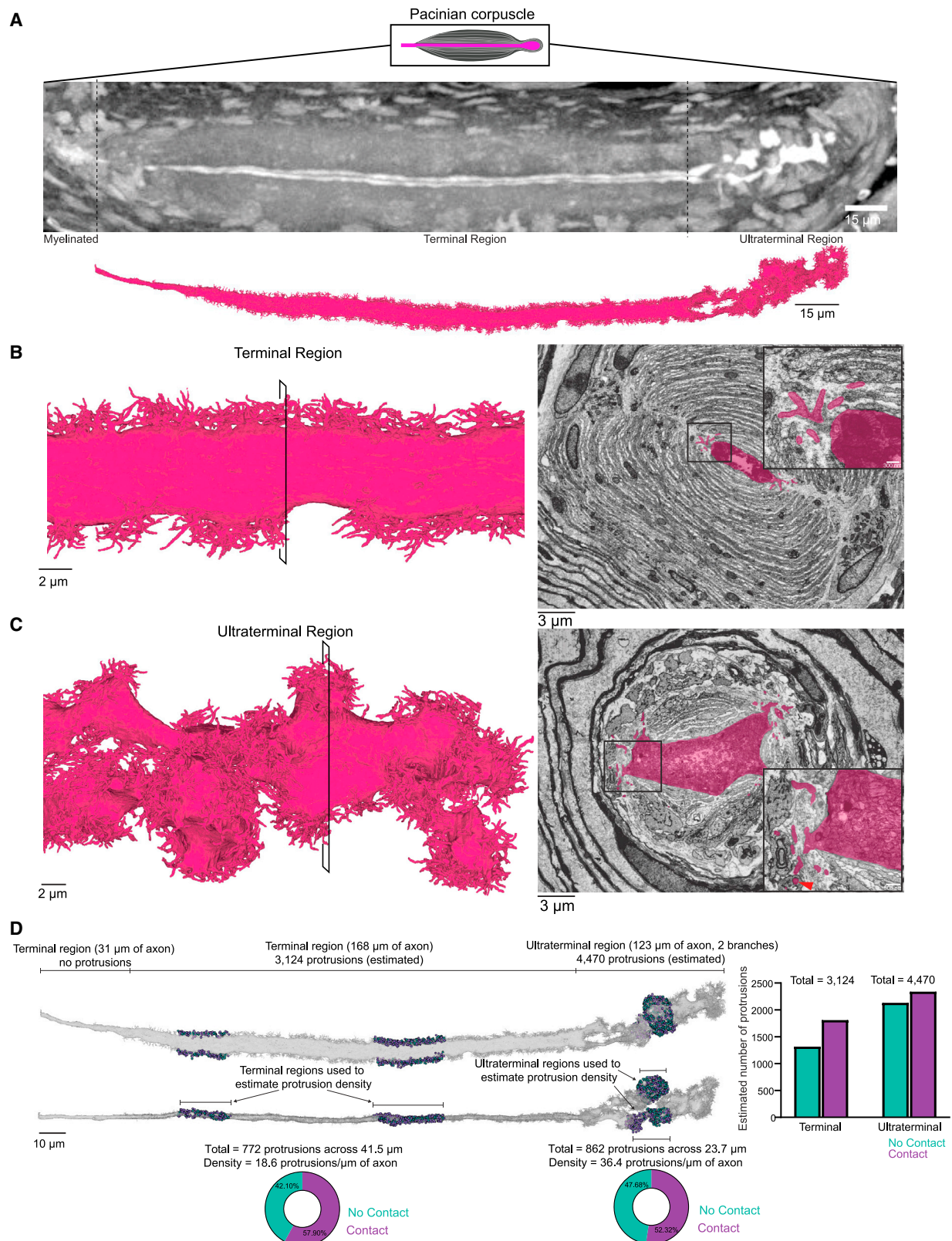
To better appreciate the quantitative form of these axon protrusions that are a conserved ultrastructural feature across the highly sensitive A $\beta$  LTMRs with RA responses (Figure 8A, reconstructions are displayed on the same scale), we performed a morphometric analysis on a subset of axon protrusions along the A $\beta$  LTMR sensory axons of each end organ type, including the lanceolate endings of the guard hair, the Ret<sup>+</sup> and TrkB<sup>+</sup> axons of the dual-innervated Meissner corpuscle, and the sensory axon of the Pacinian corpuscle volume (Figure S8A). In general, the length of protrusions along the lanceolate endings and within the ultraterminal region of the Pacinian corpuscle were longer and the surface area of lanceolate ending protrusions was larger than those of the other sensory axons (Figures S8B and S8C); however, the functional significance of these small differences is unclear. In contrast, the notably high protrusion density and complex branching patterns of the Pacinian corpuscle axonal protrusions (Figures S8D and S8E) suggest that the spatial compactness of these ultrastructures may contribute to the unique high-frequency vibration sensitivity of this end organ structure.

### Axon protrusions form cell junctions with non-neuronal cells across the three end organs

Across the three A $\beta$  RA-LTMR end organs, we found that axon protrusions formed intimate associations with neighboring lamella or TSC processes, raising the possibility of physical contact points that tether the sensory axons to non-neuronal cells across the structure of each end organ. To further assess the ultrastructural nature of these intimate associations between axon protrusions and neighboring cells, we prepared high-resolution TEM samples of each end organ using tannic acid, which enhances visualization of extracellular matrix components and identification of intercellular junctional complexes, such as adherens junctions.<sup>21</sup> Across the three end organs, we observed an abundance of fine filament-like structures and cytoplasmic densities that bridged the 15–20 nm gap between the membranes of sensory axons and their associated non-neuronal cells. These structures, which appeared structurally similar to adherens junctions, formed along the main body of the axon and neighboring TSC or lamellar cells, as has been observed previously in the hair follicles of rats,<sup>65,66</sup> and on the axon protrusions at sites of contact with non-neuronal cells (Figure 8B). Thus, axon protrusions not only greatly expand the axon surface area and allow for more expansive localization of Piezo2 across the sensory end organ, but they also anchor the sensory axon to

(C) Left: 3D renderings of the two A $\beta$  LTMRs and four lamellar cells that form the Meissner corpuscle. Right: pseudo-colored images from the FIB-SEM volume at different depths across the corpuscle. Arrowheads show points where axon protrusions contact lamellar cells.

(D) Left: 3D renderings of the two axons from the dual-innervated corpuscle and of the axon from the single-innervated corpuscle. Teal dots indicate protrusions that terminate in the collagen network (no contact). Purple dots indicate protrusions that contact lamellar cells. Right: quantification of protrusion terminals. See also Figure S6.



(legend on next page)

non-neighboring cell processes via cell-cell junctions, which physically integrate the sensory axon into the end organ microenvironment.

## DISCUSSION

Our high-resolution reconstructions of the hair follicle lanceolate complex, Meissner corpuscle, and Pacinian corpuscle, and our analysis of their ultrastructural features and their subcellular distribution of Piezo2, reveal a unified model to explain A $\beta$  RA-LTMR responsiveness and entrainment to dynamic stimuli across the morphologically dissimilar end organs of touch. We propose that like the hooks of Velcro or the burrs on the burdock plant, the elaborate protrusions of A $\beta$  RA-LTMR axons (Figure 8A) and their capacity to form adherens junctions with non-neuronal cells serve to fasten or anchor the sensory axon to numerous, distant locations and extend the reach of axonal Piezo2 across the end organ structure. This conserved ultrastructural feature allows deflection of hair or indentation or vibration of skin to stretch the axon membrane across hundreds to thousands of locations within an individual end organ structure, leading to gating of axonal Piezo2 and neuronal excitation (Figure 8C).

We found that Piezo2 localization in all three A $\beta$  RA-LTMRs is restricted to terminal axons embedded within their respective end organs. The restricted localization of Piezo2 to the sensory axons and the lack of light-touch responses in Piezo2 knockout animals,<sup>26,27,29,30</sup> but not in *Dhh-Cre; Piezo2<sup>fl/fl</sup>* mice (Figures 2A–2E), emphasizes the indispensable, cell-autonomous role of axonal Piezo2 in light touch; however, it remains possible that TSCs and lamellar cells express other mechanosensitive ion channels that modulate the tactile responses of A $\beta$  RA-LTMRs. By reconstructing the end organ-innervating regions of axons containing Piezo2, we were able to characterize ultrastructural features unique to A $\beta$  RA-LTMRs that may underlie their responsiveness to dynamic stimuli. Despite the dissimilar microenvironments in which each A $\beta$  RA-LTMR resides—neighboring a hair follicle, associated with a bone, or wedged within a dermal papilla near the surface of glabrous skin—we observed remarkable ultrastructural homology across these three end organ structures. We found an abundance of axon protrusions to be a unique structural feature conserved across the A $\beta$  RA-LTMRs within each end organ structure. Our observation that a large portion of the A $\beta$  RA-LTMR axon protrusions contact non-neuronal cells and form cell-cell junctions suggests a tether-like function for these axonal structures first described

over 50 years ago.<sup>23,44–47</sup> Although our FIB-SEM volume did not contain A $\beta$  SA-LTMRs, which form the crown-like touch dome, previous ultrastructural analysis suggests that the terminal nerve plate of A $\beta$  SA-LTMRs is smooth and lacks any discernable protrusion-like structures.<sup>20</sup> Collectively, this suggests that these axon protrusions and their tethers are ultrastructural features reserved for the most-sensitive sensory neurons involved in detecting dynamic touch.

Mechanical cell-cell coupling stabilizes tissue architecture and enables cells to sense and respond to tensile and shear forces in their microenvironment.<sup>67</sup> The abundance of junctions along the Piezo2-enriched region of A $\beta$  sensory axons suggests that they play a central role in transforming mechanical stress across the end organ structure into sensory axon membrane strain, resulting in Piezo2 activation. We observed adherens junctions joining the main body of the sensory axon to its most proximate TSC or lamellar processes as well as at contact points between axon protrusions and more distant non-neuronal cell processes. We speculate that these junctions along the axon body and protrusions act as anchor points that enhance the transmission of forces from more peripheral portions of the end organ to the central axon body, helping to explain the low-threshold responses of A $\beta$  RA-LTMRs. We found that in the hair follicle, ~50% of protrusions from A $\beta$  RA-LTMRs surrounding the guard hair extend beyond the longitudinal collagen network and enter the circumferential collagen matrix. Of the 880 protrusions that bridged these perpendicular collagen networks, over half form intimate contacts with cell processes embedded within the circumferential collagen matrix. These contacts anchor the protrusions within the circumferential collagen matrix, which may result in the unique sensitivity of the sensory axons to the shear, compressive, tensile, and torsional stress that occurs during hair deflection or nearby skin indentation (Figure 8C). A majority of these contacts in the circumferential collagen network are made with a previously unidentified cell type, which we term the circumferential support cell or CSC, revealing a novel cellular component of lanceolate ending structure and possibly function. Previous work has shown that N-cadherin localizes to the cell-cell junctions that form between the sensory axons and adjacent TSCs of rat hair follicles.<sup>66</sup> Whether N-cadherin is required for adherens junctions that form along the protrusions and within the circumferential collagen matrix described here and the role of N-cadherin in mechanotransduction of A $\beta$  RA-LTMRs remain to be explored.

In the Meissner corpuscle and Pacinian corpuscle, we speculate that tactile forces induce maximal bending and strain along

### Figure 7. FIB-SEM reconstruction of a Pacinian corpuscle A $\beta$ RA-LTMR reveals dense networks of axon protrusions that form contacts with lamellar cells

(A) X-ray tomography of a Pacinian corpuscle (axon in white) prior to FIB-SEM imaging (top) and 3D rendering of the reconstructed Pacinian A $\beta$  RA-LTMR after imaging (bottom).

(B) Left: 3D rendering of a section of the A $\beta$  RA-LTMR in the terminal region. Right: pseudo-colored image from the FIB-SEM volume with inset showing protrusions and their contacts with lamellar cells.

(C) Same as in (B) except for the ultraterminal region. The red arrowhead indicates a protrusion encased by a lamellar cell at the inner and outer core boundary.

(D) Characterization of protrusion terminals in the terminal and ultraterminal region. Two representative regions in the terminal and ultraterminal region (total of 4) were selected to quantify and characterize protrusion terminals. The pie charts show the percentage of protrusions within these regions that contact a lamellar cell (purple) or do not form a contact (teal). The statistics of protrusion terminals in these regions were used to estimate the total number of protrusions and their termination type within both the terminal and ultraterminal regions (graphed on the right).

See also Figure S7.



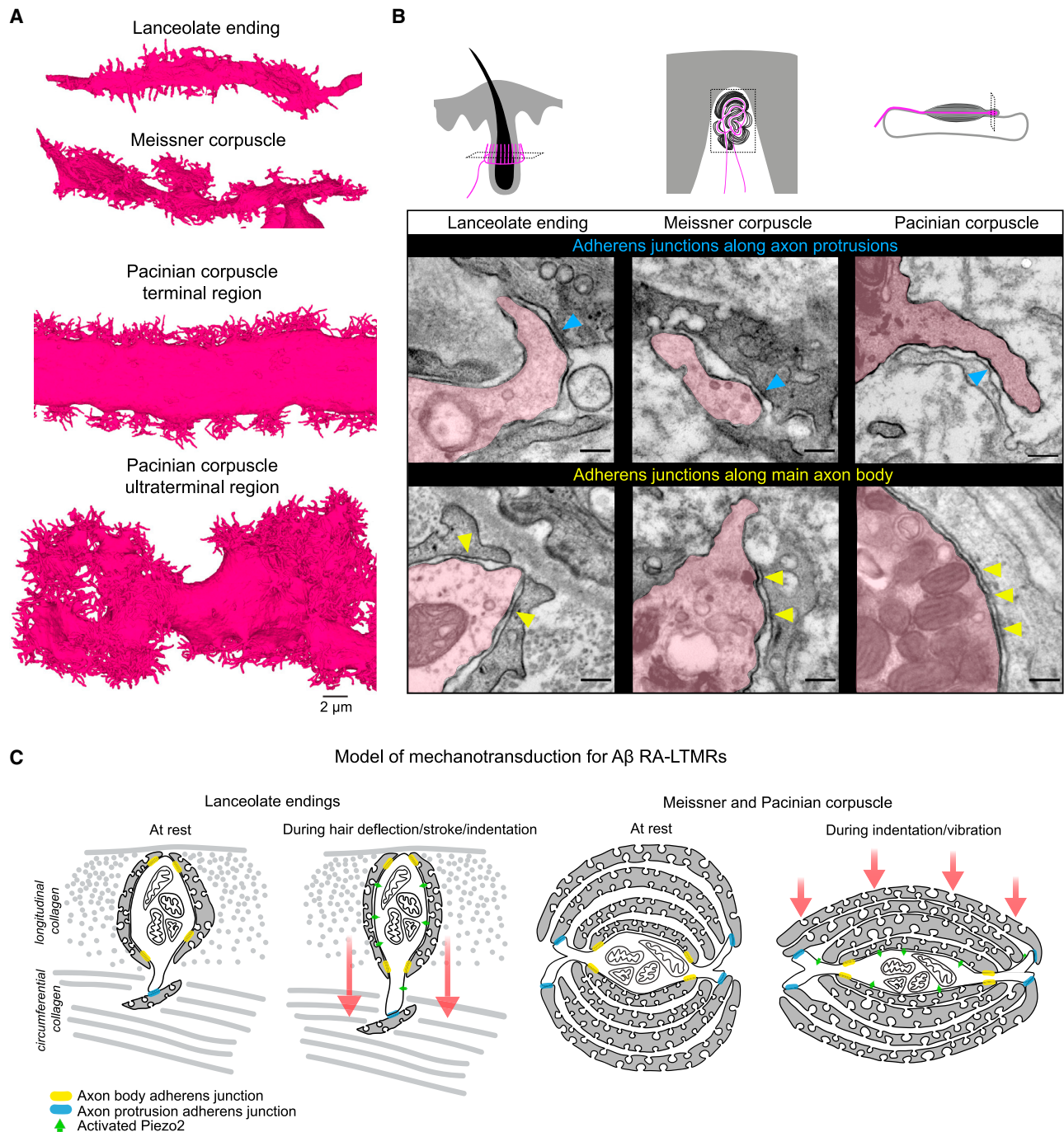


**Figure 8. The conserved presence of adherens junctions along axon protrusion contacts with non-neuronal cells and a unified model of mechanotransduction**

(A) 3D renderings of a portion of the A $\beta$  RA-LTMR axons from each end organ (terminal and ultraterminal regions shown for the Pacian corpuscle). Images are shown on the same scale.

(B) Transmission electron micrographs processed with tannic acid and post-stain showing adherens junctions between axon protrusions of A $\beta$  RA-LTMRs (magenta) and resident non-neuronal cells (blue arrowheads) and along the main body of the A $\beta$  RA-LTMRs and neighboring TSCs or lamellar cells (yellow arrowheads) in each end organ. This experiment was repeated in two animals. Scale bar, 200 nm.

(C) Schematic of proposed model of mechanotransduction for A $\beta$  RA-LTMRs. Adherens junctions serve as anchor sites that render the A $\beta$  RA-LTMR uniquely sensitive to dynamic stimuli. Hair deflection or skin indentation/vibration tugs on hundreds to thousands of protrusions along the length of the axon within the end organ, leading to stretching of the A $\beta$  RA-LTMR membrane and activation of Piezo2.

See also Figure S8.



the axon protrusions extending into the collagen network (Figure 8C). These forces may be effectively transferred to the main body of the axon as a result of the cell-cell junctions formed between the extensive array of axon protrusions and distant lamellar cell processes. In the Meissner corpuscle, we found that the more-sensitive TrkB<sup>+</sup> A $\beta$  RA-LTMR exhibited twice the number of protrusions and four times the protrusion density compared to the less-sensitive Ret<sup>+</sup> sensory axon. While an equal proportion of protrusions from the two sensory neuron types formed contacts with lamellar cells within the corpuscle, we suspect that the higher density of protrusions of the TrkB<sup>+</sup> axon render it more sensitive to dynamic, tactile stimulation. Our reconstruction of the Pacinian corpuscle, and specifically of the ultraterminal region, revealed the densest array of axon protrusions among the A $\beta$  RA-LTMRs (Figures S8D and S8E). The Pacinian corpuscle is unique among LTMR end organs in its high-pass frequency tuning. We speculate that the extensive axon protrusions and their elaborate lamellar cell contacts, together with the unique resonance properties of this end organ and the remarkably high density of axonal mitochondria, underlie the Pacinian A $\beta$  RA-LTMR's capacity to entrain to high-frequency mechanical stimuli.

Collectively, our high-resolution A $\beta$  RA-LTMR end organ architecture analyses show axon protrusions and their intimate contacts with resident, non-neuronal cells to be a common ultrastructural motif that we propose underlies the low-force threshold activation of A $\beta$  RA-LTMR axon membrane-bound Piezo2. We observed a similar motif in lanceolate endings surrounding non-guard hairs, which are also innervated by comparably sensitive low-threshold A $\delta$ - and C-LTMR sensory neurons<sup>8</sup> that also respond to dynamic touch, suggesting that these axon protrusions and their non-neuronal contacts are a conserved feature of ultrasensitive low-threshold mechanoreceptors that innervate specialized end organ structures involved in the detection of dynamic, light touch. Furthermore, given the structural homology of hair follicle lanceolate endings, Meissner corpuscles, and Pacinian corpuscles across species, we speculate that A $\beta$  RA-LTMR end organ axon protrusions and the adherens junctions they form with surrounding support cells represent a basic functional unit of mechanotransduction in humans as well.

## STAR★METHODS

Detailed methods are provided in the online version of this paper and include the following:

- **KEY RESOURCES TABLE**
- **RESOURCE AVAILABILITY**
  - Lead contact
  - Material availability
  - Data and code availability
- **EXPERIMENTAL MODEL AND SUBJECT DETAILS**
- **METHODS DETAILS**
  - Immunofluorescent staining
  - Electron microscopy sample preparation
  - Enhanced FIB-SEM sample preparation
  - Enhanced FIB-SEM 3D large volume imaging
  - Global image alignment and processing

- Automated segmentation and reconstruction
- Immunoelectron microscopy sample preparation
- Quantification of immunoelectron microscopy signal
- Quantification of lamellar cell wrappings
- Protrusion ending quantification
- Morphometric analysis of axon protrusions
- *In vivo* DRG electrophysiology
- DRG electrophysiology analysis
- Open field and balance beam behavior analysis
- **QUANTIFICATION AND STATISTICAL ANALYSIS**
- **ADDITIONAL RESOURCES**

## SUPPLEMENTAL INFORMATION

Supplemental information can be found online at <https://doi.org/10.1016/j.neuron.2023.08.023>.

## ACKNOWLEDGMENTS

We thank Maria Ericsson, Giovanni De Nola, and Shachar Dagan for advice and help with EM preparations. We thank Caiying Guo from the Janelia Research Campus for generating the *Piezo2<sup>smFP-FLAG</sup>* mouse. We thank Harald F. Hess and Adam Hantman for early input on this project. We thank Soha Ashrafi, Alan Emanuel, Vanessa Ruta, and members of the Ginty lab for comments on the manuscript. This work was supported by NIH grants NS097344 (D.D.G.) and MH117808 (W.-C.A.L.), the Edward R. and Anne G. Lefler Center for Neurodegenerative Disorders (D.D.G.), a Howard Hughes Medical Institute-Jane Coffin Childs Fellowship (A.H.), the Howard Hughes Medical Institute (D.D.G., S.P., and C.S.X.), and a Stuart H.Q. & Victoria Quan Fellowship (Q.Z.). Portions of the work were supported by a Foundry Award for the HMS Connectomics Core. D.D.G. is an investigator of the Howard Hughes Medical Institute. This article is subject to HHMI's Open Access to Publications policy. HHMI lab heads have previously granted a nonexclusive CC BY 4.0 license to the public and a sublicensable license to HHMI in their research articles. Pursuant to those licenses, the author-accepted manuscript of this article can be made freely available under a CC BY 4.0 license immediately upon publication.

## AUTHOR CONTRIBUTIONS

A.H., Q.Z., S.P., C.S.X., and D.D.G. conceived the study. A.H. and Q.Z., with the help of M.I., M.N.-T., and S.C., prepared all EM samples. S.P. and C.S.X. prepared and imaged FIB-SEM samples. Post-data registration and supervision of FIB-SEM samples were performed by C.S.X. Global image alignment and processing were performed by Q.Z. and A.H. Network training and automatic segmentation was done by T.M.N. under the supervision of W.-C.A.L. Ground truth for FIB-SEM volumes was annotated by R.P., B.S., K.A., A.S., B.B., M.K., N.A., S.C., A.H., and Q.Z. Model proofreading was performed by A.H., Q.Z., and M.N.-T. Figure S1A was created by A.H. Figures S1B, S1C, and 2A–2E were created by J.T. Open field and balance beam behavior assays were performed by M.M.D. Preliminary experiments related to study were performed by W.X., E.C.P., S.C., G.R., and C.S. A.H. and D.D.G. wrote the paper with input from all authors.

## DECLARATION OF INTERESTS

C.S.X. is the inventor of a US patent assigned to HHMI for the enhanced FIB-SEM systems used in this work: Xu, C.S., Hayworth, K.J., and Hess, H.F. (2020) Enhanced FIB-SEM systems for large-volume 3D imaging. US Patent 10,600,615, 24 Mar. 2020.

## INCLUSION AND DIVERSITY

We support inclusive, diverse, and equitable conduct of research.

Received: May 5, 2023  
Revised: July 31, 2023  
Accepted: August 22, 2023  
Published: September 18, 2023

## REFERENCES

- Handler, A., and Ginty, D.D. (2021). The mechanosensory neurons of touch and their mechanisms of activation. *Nat. Rev. Neurosci.* 22, 521–537. <https://doi.org/10.1038/s41583-021-00489-x>.
- Bai, L., Lehnert, B.P., Liu, J., Neubarth, N.L., Dickendesh, T.L., Nwe, P.H., Cassidy, C., Woodbury, C.J., and Ginty, D.D. (2015). Genetic Identification of an Expansive Mechanoreceptor Sensitive to Skin Stroking. *Cell* 163, 1783–1795. <https://doi.org/10.1016/j.cell.2015.11.060>.
- Neubarth, N.L., Emanuel, A.J., Liu, Y., Springel, M.W., Handler, A., Zhang, Q., Lehnert, B.P., Guo, C., Orefice, L.L., Abdelaziz, A., et al. (2020). Meissner corpuscles and their spatially intermingled afferents underlie gentle touch perception. *Science* 368, eabb2751. <https://doi.org/10.1126/science.abb2751>.
- Lewin, G.R., and McMahon, S.B. (1991). Physiological properties of primary sensory neurons appropriately and inappropriately innervating skin in the adult rat. *J. Neurophysiol.* 66, 1205–1217. <https://doi.org/10.1152/jn.1991.66.4.1205>.
- Koltzenburg, M., Stucky, C.L., and Lewin, G.R. (1997). Receptive properties of mouse sensory neurons innervating hairy skin. *J. Neurophysiol.* 78, 1841–1850. <https://doi.org/10.1152/jn.1997.78.4.1841>.
- Johansson, R.S., Vallbo, Å.B., and Westling, G. (1980). Thresholds of mechanosensitive afferents in the human hand as measured with von Frey hairs. *Brain Res.* 184, 343–351. [https://doi.org/10.1016/0006-8993\(80\)90803-3](https://doi.org/10.1016/0006-8993(80)90803-3).
- Cain, D.M., Khasabov, S.G., and Simone, D.A. (2001). Response properties of mechanoreceptors and nociceptors in mouse glabrous skin: An in vivo study. *J. Neurophysiol.* 85, 1561–1574. <https://doi.org/10.1152/jn.2001.85.4.1561>.
- Li, L., Rutlin, M., Abaira, V.E., Cassidy, C., Kus, L., Gong, S., Jankowski, M.P., Luo, W., Heintz, N., Koerber, H.R., et al. (2011). The Functional Organization of Cutaneous Low-Threshold Mechanosensory Neurons. *Cell* 147, 1615–1627. <https://doi.org/10.1016/j.cell.2011.11.027>.
- Werner, G., and Mountcastle, V.B. (1965). Neural activity in mechanoreceptive cutaneous afferents: Stimulus-response relations, Weber functions, and information transmission. *J. Neurophysiol.* 28, 359–397. <https://doi.org/10.1152/jn.1965.28.2.359>.
- Knibestöl, M., and Vallbo, A.B. (1980). Intensity of sensation related to activity of slowly adapting mechanoreceptive units in the human hand. *J. Physiol.* 300, 251–267. <https://doi.org/10.1113/jphysiol.1980.sp013160>.
- Coleman, G.T., Bahramali, H., Zhang, H.Q., and Rowe, M.J. (2001). Characterization of tactile afferent fibers in the hand of the marmoset monkey. *J. Neurophysiol.* 85, 1793–1804. <https://doi.org/10.1152/jn.2001.85.5.1793>.
- Harrington, T., and Merzenich, M.M. (1970). Neural coding in the sense of touch: Human sensations of skin indentation compared with the responses of slowly adapting mechanoreceptive afferents innervating the hairy skin of monkeys. *Exp. Brain Res.* 10, 251–264. <https://doi.org/10.1007/BF00235049>.
- Brown, A.G., and Iggo, A. (1967). A quantitative study of cutaneous receptors and afferent fibres in the cat and rabbit. *J. Physiol.* 193, 707–733. <https://doi.org/10.1113/jphysiol.1967.sp008390>.
- Iggo, A., and Ogawa, H. (1977). Correlative physiological and morphological studies of rapidly adapting mechanoreceptors in cat's glabrous skin. *J. Physiol.* 266, 275–296.
- Talbot, W.H., Darian-Smith, I., Kornhuber, H.H., and Mountcastle, V.B. (1968). The sense of flutter-vibration: comparison of the human capacity with response patterns of mechanoreceptive afferents from the monkey hand. *J. Neurophysiol.* 31, 301–334. <https://doi.org/10.1152/jn.1968.31.2.301>.
- Mountcastle, V.B., Talbot, W.H., Darian-Smith, I., and Kornhuber, H.H. (1967). Neural basis of the sense of flutter-vibration. *Science* 155, 597–600. <https://doi.org/10.1126/science.155.3762.597>.
- Vallbo, A.B., and Johansson, R.S. (1984). Properties of cutaneous mechanoreceptors in the human hand related to touch sensation. *Hum. Neurobiol.* 3, 3–14.
- Roe, A., Friedman, R., and Chen, L. (2007). Multiple Representation in Primate SI: A View from a Window on the Brain. In *Handbook of Neurochemistry and Molecular Neurobiology: Sensory Neurochemistry*, A. Lajtha and D.A. Johnson, eds. (Springer New York), pp. 1–16. <https://doi.org/10.1007/978-0-387-30374-1>.
- Knibestöl, M., and Vallbo, A.B. (1970). Single Unit Analysis of Mechanoreceptor Activity from the Human Glabrous Skin. *Acta Physiol. Scand.* 80, 178–195. <https://doi.org/10.1111/j.1748-1716.1970.tb04783.x>.
- Iggo, A., and Muir, A. (1969). The structure and function of a slowly adapting touch corpuscle in hairy skin. *The Journal of physiology* 188, 763–796.
- Li, L., and Ginty, D.D. (2014). The structure and organization of lanceolate mechanosensory complexes at mouse hair follicles. *Elife* 3, e01901. <https://doi.org/10.7554/elife.01901>.
- Yamamoto, T. (1966). The fine structure of the palisade-type sensory endings in relation to hair follicles. *J. Electron. Microsc.* 15, 158–166. <https://doi.org/10.1093/oxfordjournals.jmicro.a049523>.
- Halata, Z. (1993). Sensory innervation of the hairy skin (light and electronmicroscopic study). *J. Invest. Dermatol.* 101, 75S–81S. [https://doi.org/10.1016/0022-202X\(93\)90505-C](https://doi.org/10.1016/0022-202X(93)90505-C).
- Halata, Z., and Munger, B.L. (1980). Sensory nerve endings in rhesus monkey sinus hairs. *J. Comp. Neurol.* 192, 645–663. <https://doi.org/10.1002/cne.901920403>.
- Johansson, R.S., and Vallbo, A.B. (1979). Tactile sensibility in the human hand: relative and absolute densities of four types of mechanoreceptive units in glabrous skin. *J. Physiol.* 286, 283–300. <https://doi.org/10.1113/jphysiol.1979.sp012619>.
- Ranade, S.S., Woo, S.H., Dubin, A.E., Moshourab, R.A., Wetzel, C., Petrus, M., Mathur, J., Bégy, V., Coste, B., Mainquist, J., et al. (2014). Piezo2 is the major transducer of mechanical forces for touch sensation in mice. *Nature* 516, 121–125. <https://doi.org/10.1038/nature13980>.
- von Buchholtz, L.J., Ghitani, N., Lam, R.M., Licholai, J.A., Chesler, A.T., and Ryba, N.J.P. (2021). Decoding Cellular Mechanisms for Mechanosensory Discrimination. *Neuron* 109, 285–298.e5. <https://doi.org/10.1016/j.neuron.2020.10.028>.
- Chesler, A.T., Szczot, M., Bharucha-Goebel, D., Čeko, M., Donkervoort, S., Laubacher, C., Hayes, L.H., Alter, K., Zampieri, C., Stanley, C., et al. (2016). The role of PIEZO2 in human mechanosensation. *N. Engl. J. Med.* 375, 1355–1364. <https://doi.org/10.1056/NEJMoa1602812>.
- Lehnert, B.P., Santiago, C., Huey, E.L., Emanuel, A.J., Renauld, S., Africawala, N., Alkisar, I., Zheng, Y., Bai, L., Koutsoumpa, C., et al. (2021). Mechanoreceptor synapses in the brainstem shape the central representation of touch. *Cell* 184, 5608–5621.e18. <https://doi.org/10.1016/j.cell.2021.09.023>.
- Chirila, A.M., Rankin, G., Tseng, S.Y., Emanuel, A.J., Chavez-Martinez, C.L., Zhang, D., Harvey, C.D., and Ginty, D.D. (2022). Mechanoreceptor signal convergence and transformation in the dorsal horn flexibly shape a diversity of outputs to the brain. *Cell* 185, 4541–4559.e23. <https://doi.org/10.1016/j.cell.2022.10.012>.
- Coste, B., Mathur, J., Schmidt, M., Earley, T.J., Ranade, S., Petrus, M.J., Dubin, A.E., and Patapoutian, A. (2010). Piezo1 and Piezo2 are essential components of distinct mechanically activated cation channels. *Science* 330, 55–60. <https://doi.org/10.1126/science.1193270>.
- Jin, P., Jan, L.Y., and Jan, Y.N. (2020). Mechanosensitive Ion Channels: Structural Features Relevant to Mechanotransduction Mechanisms.

- Annu. Rev. Neurosci. 43, 207–229. <https://doi.org/10.1146/annurev-neuro-070918-050509>.
33. Coste, B., Xiao, B., Santos, J.S., Syeda, R., Grandl, J., Spencer, K.S., Kim, S.E., Schmidt, M., Mathur, J., Dubin, A.E., et al. (2012). Piezo proteins are pore-forming subunits of mechanically activated channels. *Nature* 483, 176–181. <https://doi.org/10.1038/nature10812>.
34. Kefauver, J.M., Ward, A.B., and Patapoutian, A. (2020). Discoveries in structure and physiology of mechanically activated ion channels. *Nature* 587, 567–576. <https://doi.org/10.1038/s41586-020-2933-1>.
35. Ikeda, R., Cha, M., Ling, J., Jia, Z., Coyle, D., and Gu, J.G. (2014). Merkel cells transduce and encode tactile stimuli to drive  $\alpha\beta$ -Afferent impulses. *Cell* 157, 664–675. <https://doi.org/10.1016/j.cell.2014.02.026>.
36. Woo, S.H., Ranade, S., Weyer, A.D., Dubin, A.E., Baba, Y., Qiu, Z., Petrus, M., Miyamoto, T., Reddy, K., Lumpkin, E.A., et al. (2014). Piezo2 is required for Merkel-cell mechanotransduction. *Nature* 509, 622–626. <https://doi.org/10.1038/nature13251>.
37. Woo, S.-H., Lumpkin, E.A., and Patapoutian, A. (2015). Merkel cells and neurons keep in touch. *Trends Cell Biol.* 25, 74–81. <https://doi.org/10.1016/j.tcb.2014.10.003>.
38. Maksimovic, S., Nakatani, M., Baba, Y., Nelson, A.M., Marshall, K.L., Wellnitz, S.A., Firozi, P., Woo, S.H., Ranade, S., Patapoutian, A., and Lumpkin, E.A. (2014). Epidermal Merkel cells are mechanosensory cells that tune mammalian touch receptors. *Nature* 509, 617–621. <https://doi.org/10.1038/nature13250>.
39. Nakatani, M., Maksimovic, S., Baba, Y., and Lumpkin, E.A. (2015). Mechanotransduction in epidermal Merkel cells. *Pflügers Arch.* 467, 101–108. <https://doi.org/10.1007/s00424-014-1569-0>.
40. Viswanathan, S., Williams, M.E., Bloss, E.B., Stasevich, T.J., Speer, C.M., Nern, A., Pfeiffer, B.D., Hooks, B.M., Li, W.P., English, B.P., et al. (2015). High-performance probes for light and electron microscopy. *Nat. Methods* 12, 568–576. <https://doi.org/10.1038/nmeth.3365>.
41. Abdo, H., Calvo-Enrique, L., Lopez, J.M., Song, J., Zhang, M.D., Usoskin, D., El Manira, A., Adameyko, I., Hjerling-Leffler, J., and Ernfors, P. (2019). Specialized cutaneous schwann cells initiate pain sensation. *Science* 365, 695–699. <https://doi.org/10.1126/science.aax6452>.
42. Nikolaev, Y.A., Feketa, V.V., Anderson, E.O., Schneider, E.R., Gracheva, E.O., and Bagriantsev, S.N. (2020). Lamellar cells in Pacinian and Meissner corpuscles are touch sensors. *Sci. Adv.* 6, eabe6393.
43. Schwaller, F., Bégay, V., García-García, G., Taberner, F.J., Moshourab, R., McDonald, B., Docter, T., Kühnemund, J., Ojeda-alonso, J., Paricio-montesinos, R., et al. (2021). USH2A is a Meissner's corpuscle protein necessary for normal vibration sensing in mice and humans. *Nat. Neurosci.* 24, 74–81. <https://doi.org/10.1038/s41593-020-00751-y>.
44. Andres, K.H. (1966). Über die Feinstruktur der Rezeptoren an Sinushaaren. *Z. Zellforsch. Mikrosk. Anat.* 75, 339–365. <https://doi.org/10.1007/BF00407165>.
45. Takahashi-Iwanaga, H. (2000). Three-dimensional microanatomy of longitudinal lanceolate endings in rat vibrissae. *J. Comp. Neurol.* 426, 259–269. [https://doi.org/10.1002/1096-9861\(20001016\)426:2<259::AID-CNE7>3.0.CO;2-N](https://doi.org/10.1002/1096-9861(20001016)426:2<259::AID-CNE7>3.0.CO;2-N).
46. Spencer, P.S., and Schaumburg, H.H. (1973). An ultrastructural study of the inner core of the Pacinian corpuscle. *J. Neurocytol.* 2, 217–235. <https://doi.org/10.1007/BF01474721>.
47. Takahashi-Iwanaga, H., and Shimoda, H. (2003). The three-dimensional microanatomy of Meissner corpuscles in monkey palmar skin. *J. Neurocytol.* 32, 363–371.
48. García-Mesa, Y., García-Piqueras, J., García, B., Feito, J., Cabo, R., Cobo, J., Vega, J.A., and García-Suárez, O. (2017). Merkel cells and Meissner's corpuscles in human digital skin display Piezo2 immunoreactivity. *J. Anat.* 231, 978–989. <https://doi.org/10.1111/joa.12688>.
49. Villarino, N.W., Hamed, Y.M.F., Ghosh, B., Dubin, A.E., Lewis, A.H., Odem, M.A., Loud, M.C., Wang, Y., Servin-Vences, M.R., Patapoutian, A., and Marshall, K.L. (2023). Labeling PIEZO2 activity in the peripheral nervous system. *Neuron* 111, 2488–2501.e8. <https://doi.org/10.1016/j.neuron.2023.05.015>.
50. Pickles, J.O., Comis, S.D., and Osborne, M.P. (1984). Cross-links between stereocilia in the guinea pig organ of Corti, and their possible relation to sensory transduction. *Hear. Res.* 15, 103–112. [https://doi.org/10.1016/0378-5955\(84\)90041-8](https://doi.org/10.1016/0378-5955(84)90041-8).
51. Howard, J., and Hudspeth, A.J. (1988). Compliance of the hair bundle associated with gating of mechanoelectrical transduction channels in the Bullfrog's saccular hair cell. *Neuron* 1, 189–199. [https://doi.org/10.1016/0896-6273\(88\)90139-0](https://doi.org/10.1016/0896-6273(88)90139-0).
52. Qiu, X., and Müller, U. (2022). Sensing sound: Cellular specializations and molecular force sensors. *Neuron* 110, 3667–3687. <https://doi.org/10.1016/j.neuron.2022.09.018>.
53. Xu, C.S., Hayworth, K.J., Lu, Z., Grob, P., Hassan, A.M., García-Cerdán, J.G., Niyogi, K.K., Nogales, E., Weinberg, R.J., and Hess, H.F. (2017). Enhanced FIB-SEM systems for large-volume 3D imaging. *Elife* 6, e25916. <https://doi.org/10.7554/eLife.25916>.
54. Nguyen, T.M., Thomas, L.A., Rhoades, J.L., Ricchi, I., Yuan, X.C., Sheridan, A., Hildebrand, D.G.C., Funke, J., Regehr, W.G., and Lee, W.C.A. (2023). Structured cerebellar connectivity supports resilient pattern separation. *Nature* 613, 543–549. <https://doi.org/10.1038/s41586-022-05471-w>.
55. Kuehn, E.D., Meltzer, S., Abaira, V.E., Ho, C.Y., and Ginty, D.D. (2019). Tiling and somatotopic alignment of mammalian low-threshold mechanoreceptors. *Proc. Natl. Acad. Sci. USA* 116, 9168–9177. <https://doi.org/10.1073/pnas.1901378116>.
56. Parton, R.G., and Del Pozo, M.A. (2013). Caveolae as plasma membrane sensors, protectors and organizers. *Nat. Rev. Mol. Cell Biol.* 14, 98–112. <https://doi.org/10.1038/nrm3512>.
57. Ghitani, N., Barik, A., Szczot, M., Thompson, J.H., Li, C., Le Pichon, C.E., Krashes, M.J., and Chesler, A.T. (2017). Specialized Mechanosensory Nociceptors Mediating Rapid Responses to Hair Pull. *Neuron* 95, 944–954.e4. <https://doi.org/10.1016/j.neuron.2017.07.024>.
58. Sharma, N., Flaherty, K., Lezgyieva, K., Wagner, D.E., Klein, A.M., and Ginty, D.D. (2020). The emergence of transcriptional identity in somatosensory neurons. *Nature* 577, 392–398.
59. Qi, L., Iskols, M., Shi, D., Reddy, P., Walker, C., Lezgyieva, K., Voisin, T., Pawlak, M., Kuchroo, V.K., Chiu, I., et al. (2023). A DRG genetic toolkit reveals molecular, morphological, and functional diversity of somatosensory neuron subtypes. Preprint at bioRxiv. <https://doi.org/10.1101/2023.04.22.537932>.
60. Zhang, Q., Lee, W.C.A., Paul, D.L., and Ginty, D.D. (2019). Multiplexed peroxidase-based electron microscopy labeling enables simultaneous visualization of multiple cell types. *Nat. Neurosci.* 22, 828–839. <https://doi.org/10.1038/s41593-019-0358-7>.
61. Paré, M., Elde, R., Mazurkiewicz, J.E., Smith, A.M., and Rice, F.L. (2001). The Meissner corpuscle revisited: A multiafferented mechanoreceptor with nociceptor immunochemical properties. *J. Neurosci.* 21, 7236–7246. <https://doi.org/10.1523/jneurosci.21-18-07236.2001>.
62. Zelená, J. (1994). *Nerves and Mechanoreceptors* (Springer Dordrecht).
63. Luo, W., Enomoto, H., Rice, F.L., Milbrandt, J., and Ginty, D.D. (2009). Molecular Identification of Rapidly Adapting Mechanoreceptors and Their Developmental Dependence on Ret Signaling. *Neuron* 64, 841–856. <https://doi.org/10.1016/j.neuron.2009.11.003>.
64. Vega, J.A., Del Valle, M.E., Haro, J.J., Naves, F.J., Calzada, B., and Uribealarea, R. (1994). The inner-core, outer-core and capsule cells of the human pacinian corpuscles: An Immunohistochemical study. *Eur. J. Morphol.* 32, 11–18.
65. Kaidoh, T., and Inoué, T. (2000). Intercellular junctions between palisade nerve endings and outer root sheath cells of rat vellus hairs. *J. Comp. Neurol.* 420, 419–427. [https://doi.org/10.1002/\(SICI\)1096-9861\(20000515\)420:4<419::AID-CNE1>3.0.CO;2-3](https://doi.org/10.1002/(SICI)1096-9861(20000515)420:4<419::AID-CNE1>3.0.CO;2-3).

66. Kaidoh, T., and Inoué, T. (2008). N-Cadherin Expression in Palisade Nerve Endings of Rat Vellus Hairs. *J. Comp. Neurol.* 506, 525–534. <https://doi.org/10.1002/cne.21550>.
67. Yap, A.S., Duszyc, K., and Viasnoff, V. (2018). Mechanosensing and mechanotransduction at cell–cell junctions. *Cold Spring Harb. Perspect. Biol.* 10, a028761. <https://doi.org/10.1101/cshperspect.a028761>.
68. Huang, S., O'Donovan, K.J., Turner, E.E., Zhong, J., and Ginty, D.D. (2015). Extrinsic and intrinsic signals converge on the Runx1/CBF $\beta$  transcription factor for nonpeptidergic nociceptor maturation. *Elife* 4, e10874. <https://doi.org/10.7554/eLife.10874>.
69. Choi, S., Hachisuka, J., Brett, M.A., Magee, A.R., Omori, Y., Iqbal, N.U.A., Zhang, D., DeLisle, M.M., Wolfson, R.L., Bai, L., et al. (2020). Parallel ascending spinal pathways for affective touch and pain. *Nature* 587, 258–263. <https://doi.org/10.1038/s41586-020-2860-1>.
70. Nonomura, K., Woo, S.H., Chang, R.B., Gillich, A., Qiu, Z., Francisco, A.G., Ranade, S.S., Liberles, S.D., and Patapoutian, A. (2017). Piezo2 senses airway stretch and mediates lung inflation-induced apnoea. *Nature* 541, 176–181. <https://doi.org/10.1038/nature20793>.
71. Kuan, A.T., Phelps, J.S., Thomas, L.A., Nguyen, T.M., Han, J., Chen, C.L., Azevedo, A.W., Tuthill, J.C., Funke, J., Cloetens, P., et al. (2020). Dense neuronal reconstruction through X-ray holographic nano-tomography. *Nat. Neurosci.* 23, 1637–1643. <https://doi.org/10.1038/s41593-020-0704-9>.
72. Jorstad, A., Nigro, B., Cali, C., Wawrzyniak, M., Fua, P., and Knott, G. (2015). NeuroMorph: A Toolset for the Morphometric Analysis and Visualization of 3D Models Derived from Electron Microscopy Image Stacks. *Neuroinformatics* 13, 83–92. <https://doi.org/10.1007/s12021-014-9242-5>.
73. Jorstad, A., Blanc, J., and Knott, G. (2018). NeuroMorph: A Software Toolset for 3D Analysis of Neurite Morphology and Connectivity. *Front. Neuroanat.* 12, 59. <https://doi.org/10.3389/fnana.2018.00059>.
74. Xu, C.S., Pang, S., Hayworth, K.J., and Hess, H.F. (2020). Transforming FIB-SEM Systems for Large-Volume Connectomics and Cell Biology. In *Volume Microscopy*, I. Wacker, E. Hummel, S. Burgold, and R. Schröder, eds. (Humana), pp. 221–243. [https://doi.org/10.1007/978-1-0716-0691-9\\_12](https://doi.org/10.1007/978-1-0716-0691-9_12).
75. Xu, C.S., Pang, S., Shtengel, G., Müller, A., Ritter, A.T., Hoffman, H.K., Takemura, S.Y., Lu, Z., Pasolli, H.A., Iyer, N., et al. (2021). An open-access volume electron microscopy atlas of whole cells and tissues. *Nature* 599, 147–151. <https://doi.org/10.1038/s41586-021-03992-4>.
76. Mallon, B.S., Shick, H.E., Kidd, G.J., and Macklin, W.B. (2002). Proteolipid promoter activity distinguishes two populations of NG2-positive cells throughout neonatal cortical development. *J. Neurosci.* 22, 876–885. <https://doi.org/10.1523/jneurosci.22-03-00876.2002>.
77. Doerflinger, N.H., Macklin, W.B., and Popko, B. (2003). Inducible site-specific recombination in myelinating cells. *Genes* 35, 63–72. <https://doi.org/10.1002/gene.10154>.
78. Razani, B., Engelman, J.A., Wang, X.B., Schubert, W., Zhang, X.L., Marks, C.B., Macaluso, F., Russell, R.G., Li, M., Pestell, R.G., et al. (2001). Caveolin-1 Null Mice Are Viable but Show Evidence of Hyperproliferative and Vascular Abnormalities. *J. Biol. Chem.* 276, 38121–38138. <https://doi.org/10.1074/jbc.M105408200>.
79. Rutlin, M., Ho, C.Y., Abaira, V.E., Cassidy, C., Bai, L., Woodbury, C.J., and Ginty, D.D. (2014). The cellular and molecular basis of direction selectivity of A $\delta$ -LTMRs. *Cell* 159, 1640–1651. <https://doi.org/10.1016/j.cell.2014.11.038>.
80. Madisen, L., Zwingman, T.A., Sunkin, S.M., Oh, S.W., Zariwala, H.A., Gu, H., Ng, L.L., Palmiter, R.D., Hawrylycz, M.J., Jones, A.R., et al. (2010). A robust and high-throughput Cre reporting and characterization system for the whole mouse brain. *Nat. Neurosci.* 13, 133–140. <https://doi.org/10.1038/nn.2467>.
81. Livet, J., Weissman, T.A., Kang, H., Draft, R.W., Lu, J., Bennis, R.A., Sanes, J.R., and Lichtman, J.W. (2007). Transgenic strategies for combinatorial expression of fluorescent proteins in the nervous system. *Nature* 450, 56–62. <https://doi.org/10.1038/nature06293>.
82. Snippert, H.J., van der Flier, L.G., Sato, T., van Es, J.H., van den Born, M., Kroon-Veenboer, C., Barker, N., Klein, A.M., van Rheenen, J., Simons, B.D., and Clevers, H. (2010). Intestinal crypt homeostasis results from neutral competition between symmetrically dividing Lgr5 stem cells. *Cell* 143, 134–144. <https://doi.org/10.1016/j.cell.2010.09.016>.
83. Hinoi, T., Akyol, A., Theisen, B.K., Ferguson, D.O., Greenon, J.K., Williams, B.O., Cho, K.R., and Fearon, E.R. (2007). Mouse model of colonic adenoma-carcinoma progression based on somatic Apc inactivation. *Cancer Res.* 67, 9721–9730. <https://doi.org/10.1158/0008-5472.CAN-07-2735>.
84. Jaegle, M., Ghazvini, M., Mandemakers, W., Piirsoo, M., Driegen, S., Levavasseur, F., Raghoenath, S., Grosfeld, F., and Meijer, D. (2003). The POU proteins Brn-2 and Oct-6 share important functions in Schwann cell development. *Genes Dev.* 17, 1380–1391. <https://doi.org/10.1101/gad.258203>.
85. Pang, S., and Xu, C.S. (2023). Methods of enhanced FIB-SEM sample preparation and image acquisition. *Methods Cell Biol.* 177, 269–300. <https://doi.org/10.1016/bs.mcb.2023.01.019>.
86. Klein, S., Staring, M., Murphy, K., Viergever, M.A., and Pluim, J.P.W. (2010). Elastix: A toolbox for intensity-based medical image registration. *IEEE Trans. Med. Imaging* 29, 196–205. <https://doi.org/10.1109/TMI.2009.2035616>.
87. Shamonin, D.P., Bron, E.E., Lelieveldt, B.P.F., Smits, M., Klein, S., and Staring, M.; Alzheimer's Disease Neuroimaging Initiative (2013). Fast parallel image registration on CPU and GPU for diagnostic classification of Alzheimer's disease. *Front. Neuroinform.* 7, 50. <https://doi.org/10.3389/fninf.2013.00050>.
88. Phelps, J.S., Hildebrand, D.G.C., Graham, B.J., Kuan, A.T., Thomas, L.A., Nguyen, T.M., Buhmann, J., Azevedo, A.W., Sustar, A., Agrawal, S., et al. (2021). Reconstruction of motor control circuits in adult *Drosophila* using automated transmission electron microscopy. *Cell* 184, 759–774.e18. <https://doi.org/10.1016/j.cell.2020.12.013>.
89. Funke, J., Tschopp, F., Grisaitis, W., Sheridan, A., Singh, C., Saalfeld, S., and Turaga, S.C. (2019). Large Scale Image Segmentation with Structured Loss Based Deep Learning for Connectome Reconstruction. *IEEE Trans. Pattern Anal. Mach. Intell.* 41, 1669–1680. <https://doi.org/10.1109/TPAMI.2018.2835450>.
90. Boergens, K.M., Berning, M., Bocklisch, T., Bräunlein, D., Drawitsch, F., Frohnhofer, J., Herold, T., Otto, P., Rzepka, N., Werkmeister, T., et al. (2017). WebKnossos: Efficient online 3D data annotation for connectomics. *Nat. Methods* 14, 691–694. <https://doi.org/10.1038/nmeth.4331>.
91. Lee, K., Zung, J., Li, P., and Viren Jain, H.S.S. (2017). Superhuman accuracy on the SNEMI3D connectomics challenge. Preprint at arXiv. <https://doi.org/10.48550/arXiv.1706.00120>.



## STAR★METHODS

### KEY RESOURCES TABLE

REAGENT or RESOURCE	SOURCE	IDENTIFIER
<b>Antibodies</b>		
goat anti-mCherry	Sicgen	AB0040-200; RRID:AB_2333093
chicken anti-GFP	Aves lab	GFP-1020; RRID:AB_10000240
rabbit anti-GFP	Invitrogen	A-11122
goat anti-GFP	US Biological	G8965-01E
rabbit anti-S100 beta	ProteinTech	15146-1-AP; RRID:AB_2254244
rabbit anti-TUJ1 (TUBB3)	Biolegend	802001; RRID:AB_2564645
chicken anti-neurofilament heavy chain	Aves lab	SKU: NFH; RRID:AB_2313552
rabbit anti-CGRP	Immunostar	2411; RRID:AB_572217
guinea pig anti-FLAG	Huang et al. <sup>68</sup>	N/A
<b>Chemicals, peptides, and recombinant proteins</b>		
Tamoxifen	Sigma	T5648-1g
Sunflower seed oil	Sigma	S5007
Urethane	Sigma	U2500
Tannic acid low molecular weight	EMS	21710
Glutaraldehyde	EMS	16316
Paraformaldehyde	EMS	15712
Sodium cacodylate	EMS	12310
Calcium chloride	Sigma	793639
Magnesium chloride hexahydrate	Sigma	M9272
Glycine	Sigma	410225
3,3'-diaminobenzidine tetrahydrochloride hydrate	Sigma	D5637
Osmium tetroxide	EMS	19190
Potassium ferrocyanide	Sigma	P3289
Uranyl acetate	EMS	22400
Maleic acid	Sigma	M0375
Propylene oxide	EMS	20411
LX-112	Ladd Research	21310
DDSA	EMS	13710
NMA	EMS	19000
DMP-30	EMS	13600
Durcupan AMC	Sigma	44610-1EA
Gelatin from cold water fish	Sigma	G7041-100G
Normal goat serum	Vector labs	S-1000
Nanogold®-Fab' Goat anti-Guinea Pig IgG (H + L)	Nanoprobes	#2055-0.5ML
HQ Silver Enhancer	Nanoprobes	#2012-45ML
Neg-50 Frozen Section Medium	VWR	21008-918
Samarium(III) chloride	Sigma	400610
<b>Deposited data</b>		
Guard hair follicle FIB-SEM and segmentation volumes	This paper	<a href="https://openorganelle.janelia.org/datasets/jrc_mus-guard-hair-follicle">https://openorganelle.janelia.org/datasets/jrc_mus-guard-hair-follicle</a> <a href="https://doi.org/10.25378/janelia.23969052">https://doi.org/10.25378/janelia.23969052</a> , <a href="https://doi.org/10.25378/janelia.23969061">https://doi.org/10.25378/janelia.23969061</a>

(Continued on next page)

**Continued**

REAGENT or RESOURCE	SOURCE	IDENTIFIER
Single-innervated Meissner corpuscle FIB-SEM and segmentation volumes	This paper	<a href="https://openorganelle.janelia.org/datasets/jrc_mus-meissner-corpuscle-1">https://openorganelle.janelia.org/datasets/jrc_mus-meissner-corpuscle-1</a> <a href="https://doi.org/10.25378/janelia.23969070">https://doi.org/10.25378/janelia.23969070</a> , <a href="https://doi.org/10.25378/janelia.23969076">https://doi.org/10.25378/janelia.23969076</a>
Double-innervated Meissner corpuscle FIB-SEM and segmentation volumes	This paper	<a href="https://openorganelle.janelia.org/datasets/jrc_mus-meissner-corpuscle-2">https://openorganelle.janelia.org/datasets/jrc_mus-meissner-corpuscle-2</a> <a href="https://doi.org/10.25378/janelia.23969106">https://doi.org/10.25378/janelia.23969106</a> , <a href="https://doi.org/10.25378/janelia.23969109">https://doi.org/10.25378/janelia.23969109</a>
Pacinian corpuscle FIB-SEM and segmentation volumes	This paper	<a href="https://openorganelle.janelia.org/datasets/jrc_mus-pacinian-corpuscle">https://openorganelle.janelia.org/datasets/jrc_mus-pacinian-corpuscle</a> <a href="https://doi.org/10.25378/janelia.23969112">https://doi.org/10.25378/janelia.23969112</a> , <a href="https://doi.org/10.25378/janelia.23969115">https://doi.org/10.25378/janelia.23969115</a>

**Experimental models: Organisms/strains**

Mouse: <i>Piezo2</i> <sup>smFP-FLAG</sup>	This paper	By request
Mouse: <i>Plp1</i> <sup>EGFP</sup>	The Jackson Laboratory	RRID:IMSR_JAX:033357
Mouse: <i>Plp1</i> <sup>CreER</sup>	The Jackson Laboratory	RRID:IMSR_JAX:005975
Mouse: <i>ROSA26</i> <sup>LSL-Matrix-dAPEX2</sup>	The Jackson Laboratory	RRID:IMSR_JAX:032765
Mouse: <i>ROSA26</i> <sup>FSF-Matrix-dAPEX2</sup>	The Jackson Laboratory	RRID:IMSR_JAX:032766
Mouse: <i>TrkB</i> <sup>CreER</sup>	The Jackson Laboratory	RRID:IMSR_JAX:030291
Mouse: <i>CGRP</i> <sup>FlpE</sup>	Choi et al. <sup>69</sup>	N/A
Mouse: <i>Cav1</i> <sup>null</sup>	The Jackson Laboratory	RRID:IMSR_JAX:007083
Mouse: <i>TrkB</i> <sup>CreER</sup>	The Jackson Laboratory	RRID:IMSR_JAX:027214
Mouse: <i>ROSA26</i> <sup>FSF-LSL-tdTomato</sup>	The Jackson Laboratory	RRID:IMSR_JAX:021875
Mouse: <i>Advillin</i> <sup>FlpO</sup>	Choi et al. <sup>69</sup>	N/A
Mouse: <i>NPY2R-GFP</i>	GENSAT	011016-UCD
Mouse: <i>Cdx2</i> <sup>Cre</sup>	The Jackson Laboratory	RRID:IMSR_JAX:009350
Mouse: <i>Piezo2</i> <sup>fl/fl</sup>	The Jackson Laboratory	RRID:IMSR_JAX:027720
Mouse: <i>Piezo2</i> <sup>null</sup>	Nonomura et al. <sup>70</sup>	N/A
Mouse: <i>ROSA26</i> <sup>CAG-Brainbow2.1 (ROSA26-Confetti)</sup>	The Jackson Laboratory	RRID:IMSR_JAX:017492
Mouse: <i>Dhh</i> <sup>Cre</sup>	The Jackson Laboratory	RRID:IMSR_JAX:012929

**Oligonucleotides**

gRNA: CCTTAATACGACTCACTATAG GCAAACGATCACTTAAGACCTGGG TTTGTAGCTAGAAATAGC	This paper	N/A
gRNA: AAAAGCACCGACTCGGTGCC ACTTTTCAAGTTGATAACGGACTAG CCTTATTTTAACCTTGCTATTCTAGCT CTAAAC	This paper	N/A
Forward5' Piezo2-Exon54: TGGAAC GGAGGAAGACCTCTACG	This paper	N/A
Reverse5' Piezo2-smFP-FLAG: GAACA GCTCCTCGCCTTTTCG	This paper	N/A
Reverse5' Piezo2-3'UTR: CCCTGATTT CAGAGACATGGGAGT	This paper	N/A

**Software and algorithms**

MATLAB	Mathworks	RRID: SCR_001622
Python	<a href="https://www.python.org/">https://www.python.org/</a>	N/A
PRISM8	GraphPad	N/A
Segway	Nguyen et al. <sup>54</sup> ; Kuan et al. <sup>71</sup>	N/A
Gunpowder	Nguyen et al. <sup>54</sup>	<a href="https://github.com/funkey/gunpowder/">https://github.com/funkey/gunpowder/</a>

(Continued on next page)

## Continued

REAGENT or RESOURCE	SOURCE	IDENTIFIER
MD-Seg	Nguyen et al. <sup>54</sup>	<a href="https://github.com/htem/segway.mdseg">https://github.com/htem/segway.mdseg</a> , ver. 0.1
Neuroglancer	<a href="https://github.com/htem/neuroglancer_mdseg/tree/segway_pr_v2">https://github.com/htem/neuroglancer_mdseg/tree/segway_pr_v2</a> , ver 2.17; forked from <a href="https://github.com/google/neuroglancer">https://github.com/google/neuroglancer</a>	N/A
Elastix	<a href="https://github.com/SuperElastix/elastix">https://github.com/SuperElastix/elastix</a> ; <a href="https://github.com/htem/run_elastix">https://github.com/htem/run_elastix</a>	N/A
WebKnossos	<a href="https://github.com/scalableminds/webknossos">https://github.com/scalableminds/webknossos</a>	N/A
NeuroMorph	<a href="https://neuromorph.epfl.ch/">https://neuromorph.epfl.ch/</a> ; Jorstad et al. <sup>72,73</sup>	N/A
Blender	<a href="https://www.blender.org/">https://www.blender.org/</a>	N/A
Igneous	<a href="https://github.com/seung-lab/igneous">https://github.com/seung-lab/igneous</a>	N/A
Other		
Patch-clamp amplifier	Molecular Devices	Multiclamp 700A
Acquisition system	Molecular Devices	Digidata 1440A
TEM Microscope	JEOL	1200EX
FIB-SEM custom imaging system	Zeiss	Xu et al. <sup>53,74,75</sup>

## RESOURCE AVAILABILITY

### Lead contact

Further information and requests for resources and reagents should be directed to and will be fulfilled by the lead contact, David Ginty ([david\\_ginty@hms.harvard.edu](mailto:david_ginty@hms.harvard.edu)).

### Material availability

The *Piezo2<sup>smFP-FLAG</sup>* mouse line is available upon request.

### Data and code availability

All data reported in this study and code used for analysis will be shared by the [lead contact](#) upon request. All raw-aligned and segmented FIB-SEM volumes generated for this study are available through Janelia's OpenOrganelle (see [key resources table](#) for links and DOIs).

## EXPERIMENTAL MODEL AND SUBJECT DETAILS

Mice used in this study were maintained on mixed C57Bl/6J and CD1 backgrounds, except for mice used for the hair follicle (MH200121-B2K) and two Meissner corpuscle FIB-SEM samples (200913FPT and 200913FPT2), which were pure C57Bl/6J, and included both males and females. The *Piezo2<sup>smFP-FLAG</sup>* knock-in allele was generated at the Janelia Campus Research Gene Targeting and Transgenic Facility. The knock-in targeting construct was produced using recombineering techniques and traditional molecular cloning. A 5,197 bp of genomic DNA fragment containing exons 53 and 54 of the *Piezo2* gene was retrieved from BAC clone RP24-130D5. The *smFP-FLAG* gene was fused to Exon 54 followed by an frt-NeoR-frt cassette for ES cell selection. The homologous arms of the construct were 3,542 bp and 2,075 bp respectively. To facilitate ES cell targeting Crispr/cas9 system was used. gRNA was transcribed *in vitro* using MEGA shortscript T7 kit (Life Tech Corp AM1354). The template was PCR amplified using primers:

Forward 5'- CCTTAATACGACTCACTATAGGCAAAGTATGACCTTAAGACCTGGGTTTATAGAGCTAGAAATAGC -3'

Reverse 5'- AAAAGCACCGACTCGGTGCCACTTTTTCAAGTTGATAACGGACTAGCCTTATTTAACTTGCTATTTCTAGCTCTAAAC -3'

The gRNA was tested *in vitro* before being used for ES cell targeting. The test was carried out in a reaction of NEB 3.1 buffer 1  $\mu$ L, DNA template 120 ng, gRNA 40 ng, cas9 160 ng in a total volume of 10  $\mu$ L. The reaction mix was incubated at 37°C for 2 h. 0.5  $\mu$ L proteinase K (20  $\mu$ g/ $\mu$ L) was then added and incubated at 57°C for 30 min.

The targeting vector, cas9 protein (Fisher Scientific A36499 TRUECUT CAS9 PROTEIN V2) and the gRNA with concentrations of 10  $\mu$ g, 3.75  $\mu$ g and 1  $\mu$ g respectively in total volume of 100  $\mu$ L were co-electroporated into 1 million of G1 ES cells, which were derived from F1 hybrid blastocyst of 129S6 x C57Bl/6J. 74 G418 resistant ES colonies were isolated and screened by nested PCR using primers outside the construct paired with primers inside the construct. The primers used for ES cell screening were as following:

5' arm forward primers: Sptbn1 Scr F1 (5'- CGCTCACTAGAGCAAAGTTG -3') and Sptbn1 Scr F2 (5'- TAGGGTTCCTAGTAGGATCC -3'). Reverse primers: Cre scr R1 (5'- GAGGGACCTAATAACTTCGT -3') and Cre scr R2 (5'- ATGATCGGAATTGGGCTGCA -3').



3' arm forward primers: mMapple scr F1 (5'- CCATAGGATCGAGATCCTGT -3') and mMapple scr F2, (5'- GACTACAACAAGG TCAAGCTGT -3'); Reverse primers: Sptbn1 Scr R1 (5'- CAGAGCAGCAGTTCTGACTT -3') and Sptbn1 Scr 3R2 (5'- GACCCAG AGATCTAATTCC -3');

38 of 48 ES cell clones screened contained both arms. Three of them were used for making chimeric mice. Chimeric mice were generated by aggregating the ES cells with 8-cell embryos of CD-1 strain. After achieving successful germline transmission of the *Piezo2<sup>smFP-FLAG</sup>* gene in one strain, the frt-NeoR-frt cassette was excised. Proper insertion of the gene into the *Piezo2* locus was confirmed with loss of the wild-type *Piezo2* gene in a mouse homozygous for the knock-in allele using the following primers:

Forward5' *Piezo2*-Exon54: TGGAAGTGGAGGAAGACCTCTACG.

Reverse5' *Piezo2*-smFP-FLAG: GAACAGCTCCTCGCCTTTCG.

Reverse5' *Piezo2*-3'UTR: CCCTGATTCAGAGACATGGGAGT.

Mice with two copies of *Piezo2<sup>smFP-FLAG</sup>* appeared phenotypically similar to heterozygote and wild-type littermate animals. We observed no difference in distance traveled in open field or time to cross a balance beam between genetic groups (Figures S1D and S1E), suggesting that smFLAG insertion does not have a profound impact on *Piezo2*'s function. However, we did not perform single-channel recordings to assess electrophysiological differences in the tagged compared to the untagged channel.

To achieve specific labeling of sensory neuron subtypes, CreER driver lines were induced by administering tamoxifen dissolved in sunflower seed oil via intraperitoneal (I.P.) injection. Tamoxifen (MilliporeSigma) was dissolved in ethanol (MilliporeSigma) and then mixed with an equal volume of sunflower seed oil (MilliporeSigma). The mixture was vortexed, and ethanol was then removed under vacuum. The dosage for tamoxifen was as follows: for *Plp1<sup>CreER</sup>*, mice received an I.P. injection of 1 mg of tamoxifen for 5 days (P15-P19); for *TrkB<sup>CreER</sup>*, mice received an I.P. injection of 0.5 mg at P4; for *TrkC<sup>CreER</sup>*, mice received an I.P. injection of 0.5 mg of tamoxifen at P5.

*Plp1<sup>EGFP</sup>* (JAX 033357)<sup>76</sup> and *Plp1<sup>CreER</sup>* (JAX 005975)<sup>77</sup> were used to label Schwann cells. *ROSA26<sup>LSL-Matrix-dAPEX2</sup>* (JAX 032765) and *ROSA26<sup>FSF-Matrix-dAPEX2</sup>* (JAX 032766) were used for genetic EM labeling.<sup>60</sup> *TrkC<sup>CreER</sup>* (JAX 030291) was used to label A $\beta$  field LTMRs.<sup>2</sup> *CGRP<sup>FlpE</sup>* was used to label A $\delta$  HTMRs.<sup>69</sup> *Cav1<sup>null</sup>* (JAX 007083) was used to ablate caveolae.<sup>78</sup> *TrkB<sup>CreER</sup>* (JAX 027214)<sup>79</sup> together with *Advillin<sup>FlpO69</sup>* and *ROSA26<sup>FSF-LSL-tdTomato</sup>* (JAX 021875)<sup>80</sup> was used to selectively label Meissner A $\beta$  RA-LTMRs. *NPY2R-GFP* (GENSAT 011016-UCD) was used to label hairy A $\beta$  RA-LTMRs. *ROSA26<sup>CAG-Brainbow2.1</sup>* (*ROSA26-Confetti*, JAX 017492) was used to visualize different lamellar cells in the Pacinian corpuscle.<sup>81,82</sup> *Cdx2<sup>Cre</sup>* (JAX 09350) was used to delete *Piezo2* in the sensory neurons and peripheral Schwann cells.<sup>83</sup> *Piezo2<sup>null</sup>* and *Piezo2<sup>fl/fl</sup>* were used to delete *Piezo2* in a Cre-independent<sup>70</sup> and dependent manner.<sup>36</sup> *Dhh<sup>Cre</sup>* was used to delete *Piezo2* in peripheral Schwann cells (JAX 012929).<sup>84</sup> Mice were handled and housed in standard cages in accordance with the Harvard Medical School and IACUC guidelines.

## METHODS DETAILS

### Immunofluorescent staining

Tissue was isolated from P20 or older mice that were euthanized with isoflurane or sedated using a ketamine/xylazine mixture. Forepaw digit tips were cut to isolate tissue containing Meissner corpuscles. The back was treated with Nair to remove all hair and a large section of skin was cut. The fat on the underside of the hairy skin was removed to improve antibody penetration. Pacinian corpuscles were isolated from the periosteum membrane from the fibula of the mouse. The entire periosteum was isolated for whole mount staining. For staining of the Pacinian with cyrosections, *Plp1<sup>EGFP</sup>* mice were used to visualize and isolate Pacinian corpuscles in the periosteum membrane. Tissues were drop fixed in either 1% paraformaldehyde (PFA) in phosphate-buffered saline (PBS) for 1–2 h at 4°C (for more sensitive antibodies) or Zamboni's fixation buffer for 24 h at 4°C. Following fixation, all tissues were rinsed in PBS and processed for 25  $\mu$ m sections or whole mount staining as previously described.<sup>3</sup> For Figure S6F, forepaw digit tips were sectioned at 200  $\mu$ m and processed for whole mount staining. For each section, the proportion of Meissner corpuscles (labeled by S100B) that were innervated by a TrkB afferent (labeled by tdTomato) was calculated.

Primary antibodies were goat anti-mCherry (Sicgen, cat. no. AB0040-200, 1:500), chicken anti-GFP (Aves Lab, cat. no. GFP-1020, 1:500), rabbit anti-GFP (Invitrogen, cat. no. A-11122, 1:500), goat anti-GFP (US Biological, cat. no. G8965-01E, 1:500–1:1000), rabbit anti-S100 beta (ProteinTech, cat. no. 15146-1-AP, 1:300), rabbit anti-TUJ1 (Biolegend, cat. no. 802001, 1:500), chicken anti-neurofilament heavy chain (Aves, SKU: NFH, 1:300–1:500), rabbit anti-CGRP (Immunostar, cat. no. 24112, 1:375), and guinea pig anti-FLAG (1:500).<sup>68</sup> The same laser settings and contrast/brightness adjustments were made in Figures 1B and S1G to compare FLAG levels in *Piezo2<sup>smFP-FLAG</sup>* animals and littermate controls.

### Electron microscopy sample preparation

Skin/tissue regions enriched for Meissner corpuscles, hair follicles, and Pacinian corpuscles were dissected as follows for electron microscopy (EM) sample preparations. The forepaw digit tips were dissected to isolate Meissner corpuscles. For hairy skin samples, a rectangular piece of skin (~1 mm  $\times$  2 mm) was dissected with the rostral/caudal axis oriented along the long axis of the sample. For hairy skin samples that focused on the ultrastructure of an isolated guard hair, all hairs except the guard hair were trimmed in a small piece of back hairy skin, allowing us to track the location of a guard hair follicle within the sample. Non-guard hairs were identified for analysis in Figure S5D based on their smaller follicle size and ultrastructural features. Pacinian corpuscles were isolated and dissected from the periosteum membrane surrounding the fibula using the fluorescent marker *Plp1<sup>EGFP</sup>*. Tissue samples containing

forepaw digit tips, back hairy skin, and Pacinian corpuscles were immersed in a glutaraldehyde/formaldehyde fixative for 1 h at room temperature, further dissected to remove muscle and fat, and subsequently fixed overnight at 4°C. Sample preparation was done as previously described.<sup>60</sup> Ultrathin sections were cut at 50–70 nm and imaged using a JEOL 1200EX transmission electron microscope at 80 kV accelerating voltage. Images were cropped and adjusted to enhance contrast using Fiji/ImageJ. For tannic acid treatment, samples were incubated in cacodylate buffer containing 1% low molecular weight tannic acid (Electron Microscopy Sciences) for 30 min between the osmication step and the uranyl acetate step, with washes preceding and following this treatment. Ultra-thin sections were then stained with uranyl acetate and lead citrate. All single section TEM images presented in the paper were pseudo-colored by hand.

### Enhanced FIB-SEM sample preparation

Skin/tissue regions enriched for Meissner corpuscles, hair follicles, and Pacinian corpuscles were dissected as described above. Four durcupan embedded mouse end organ samples: one hair follicle sample (MH200121-B2K), two Meissner corpuscle samples (200913FPT and 200913FPT2), and one Pacinian corpuscle sample (Pacinian2A) were prepared for FIB-SEM as described previously.<sup>85</sup> Specifically, each sample was first mounted to the top of a 1 mm copper post, which was in contact with the metal-stained sample for better charge dissipation, as previously described.<sup>53</sup> The vertical sample posts were each trimmed to a small block containing the Region of Interest (ROI) with a width perpendicular to the ion beam, and a depth in the direction of the ion beam. The block sizes (width × depth) were 105 × 100 μm<sup>2</sup>, 90 × 70 μm<sup>2</sup>, and 85 × 75 μm<sup>2</sup>, and 140 × 120 μm<sup>2</sup> for MH200121-B2K, 200913FPT, 200913FPT2, and Pacinian2A respectively. The trimming was guided by X-ray tomography data obtained by a Zeiss Versa XRM-510 and optical inspection under a Leica UC7 ultramicrotome. Thin layers of conductive material of 10-nm gold followed by 100-nm carbon were coated on the trimmed samples using a Gatan 682 Precision Etching and Coating System. The coating parameters were 6 keV, 200 nA on both argon gas plasma sources, and 10 rpm sample rotation with 45-degree tilt.

### Enhanced FIB-SEM 3D large volume imaging

These four FIB-SEM prepared samples, MH200121-B2K (guard hair follicle volume), 200913FPT (single-innervated Meissner corpuscle), 200913FPT2 (dual-innervated Meissner corpuscle) and Pacinian2A (Pacinian corpuscle) were imaged by four customized Zeiss FIB-SEM systems previously described.<sup>53,74,75</sup> Each block face of ROI was imaged by a 1-nA electron beam with 0.9 keV landing energy. The x-y pixel resolution was set at 6 nm. A subsequently applied focused Ga<sup>+</sup> beam of 15 nA at 30 keV strafed across the top surface and ablated away 6 nm of the surface. The newly exposed surface was then imaged again. The hair follicle (MH200121-B2K) and Meissner corpuscle (200913FPT and 200913FPT2) samples were imaged at 1 MHz throughout their entire volumes. The ablation–imaging cycle continued about once every three and a half minutes for five weeks to complete FIB-SEM imaging MH200121-B2K, and about once every minute for one week to complete 200913FPT and 200913FPT2. To best balance the total acquisition duration and the image quality (signal to noise ratio) in critical sections, the Pacinian corpuscle sample was imaged sequentially using three different SEM scanning rates of 3 MHz, 2 MHz and 1 MHz for the top (myelinated region and part of the terminal region), middle (terminal region and part of the ultraterminal region) and bottom (ultraterminal region) sections of ROI, respectively. The ablation–imaging cycle continued about once every 50 s for 16 days to complete the top section ROI of 55 × 60 × 185 μm<sup>3</sup>, continued about once every 65 s for 9 days to complete the middle section ROI of 55 × 60 × 70 μm<sup>3</sup>, and continued about once every 2 min for 13 days to complete the bottom section ROI of 55 × 60 × 60 μm<sup>3</sup>. The entire Pacinian2A sample was FIB-SEM imaged for 38 days. Each acquired image stack formed a raw imaged volume, followed by post processing of image registration and pairwise alignment using a Scale Invariant Feature Transform (SIFT) based algorithm. The aligned stack consists of a final isotropic volume of 80 × 80 × 80 μm<sup>3</sup>, 30 × 40 × 50 μm<sup>3</sup>, 35 × 40 × 40 μm<sup>3</sup> and 55 × 60 × 291 μm<sup>3</sup> for MH200121-B2K, 200913FPT, 200913FPT2, and Pacinian2A respectively. The voxel size of 6 × 6 × 6 nm<sup>3</sup> was maintained for each sample throughout the entire volume, which can be viewed in any arbitrary orientations. 174 nm was missing in MH200121-B2K between slice 6483 and slice 6484 due to microscope issues.

### Global image alignment and processing

Three slices (7597, 7598, 7962) were discarded in MH200121-B2K due to microscope issues, and adjacent slices (7596, 7599, 7961) were copied over. For global alignment, the SIFT-aligned FIB-SEM stacks were downsampled 32x to 192 × 192 × 192 nm<sup>3</sup> voxel size and adjusted for contrast to reduce illumination unevenness. μCT volumes were cropped to just large enough to fully include the FIB-SEM ROI. The downsampled FIB-SEM stacks were used as moving images to align to μCT stacks which were fixed images using elastix.<sup>86,87</sup> The elastix alignment was done in a manner similar to Phelps et al.<sup>88</sup> ([https://github.com/htem/run\\_elastix](https://github.com/htem/run_elastix)), where an affine alignment was followed by a B-spline elastic alignment. Mutual information (AdvancedMattesMutualInformation) was used as the main metric, and 28 grid spacing and 0 bending weight was used for B-spline alignment to avoid distortions. Corresponding points were added whenever necessary. After satisfactory alignment was achieved, the transform was inverted to allow the mapping of coordinates in the SIFT-aligned FIB-SEM space to the μCT space. In order to align images by translation alone to reduce distortion, the geometric center of each section was mapped to the μCT space, given that it is rotationally invariant and in general in a well aligned region for elastix alignment. Since the z-axes were nearly identical in direction for the SIFT-aligned FIB-SEM volume and the μCT volume, these transformed coordinates can then be used as displacement vectors to align raw image stacks.

To generate the final volumes, raw FIB-SEM images were first processed to clean up milling artifacts using Fourier transform,<sup>53</sup> and then contrast enhanced using CLAHE. Images were then placed using displacement vectors generated above into an aligned volume. Volumes were rotated in 3-D space to align their z-axes to major anatomical axes, such as the hair shaft, for the ease of visualization and analysis.

### Automated segmentation and reconstruction

We used Segway, a segmentation pipeline previously developed for segmentation of transmission EM data<sup>54</sup> and later refined for X-ray and isotropic data segmentation,<sup>71</sup> to automatically segment the FIB-SEM datasets. Segway uses a 3D U-Net convolutional neural network (CNN) model to create an affinity map to predict a 'connectedness' probability of each voxel to adjacent voxels.<sup>89</sup> CNN models were trained using ground truth labels generated through manual segmentation of small image volumes that included the sensory axons, non-neuronal cells of interest, as well as "background" regions (e.g., "empty" areas that should be masked out for reconstruction) using webKnossos.<sup>90</sup> A separate CNN model was generated for each dataset using volume-specific ground truth for MH200121-B2K (guard hair follicle volume), 200913FPT2 (dual-innervated Meissner corpuscle volume), and Pacinian2A (Pacinian corpuscle volume), except for 200913FPT2 which used the same CNN model as 200913FPT2 due to their homology. For CNN training we used Gunpowder (<https://github.com/funkey/gunpowder/>) to randomly sample batches and perform data augmentation; the network architecture and training parameters are as previously described,<sup>71</sup> though in these models we also use long-range affinities<sup>91</sup> to improve prediction accuracy. After the models were trained, Daisy (<https://github.com/funkelab/daisy>) was used to deploy the CNN models and subsequent post-processing steps in the Segway pipeline to generate the output segmentation.

All volumes were segmented at  $6 \times 6 \times 6 \text{ nm}^3$  resolution except the Pacinian volume which was segmented at  $12 \times 12 \times 12 \text{ nm}^3$  to increase performance speed without a noticeable increase in error. To proofread and reconstruct neurons, we used MD-Seg, a merge-deferred segmentation proofreading method.<sup>54</sup> This method pre-agglomerates segmentation fragments only in a local block instead of across the entire volume to avoid catastrophic merge error propagations that often occur in large volumes. Inter-block merge decisions are computed and accessible to the proofreader during the reconstruction in the user interface using a hotkey. This pre-agglomeration threshold was 0.5 (out of a range from 0.0 to 1.0) for all volumes except for Pacinian2A which was 0.9 because only the axon was constructed and to minimize proofreading time of split errors.

To reconstruct the sensory neurons and non-neuronal cells of interest within our FIB-SEM volumes, we first identified the cells to be reconstructed based on their stereotypical morphological characteristics and selected a cell fragment that was contained within a single block. Using the hotkey, mergeable fragments in adjacent blocks were added to the single block from all sides. Sequential use of the hotkey enabled the proofreader to 'grow' the cell by continually adding computed merge fragments at the boundaries of the growing cell. In the event of a merge error, growth from the block containing the error could be blocked and removed from the reconstruction to prevent any further growth from the merged segment.

In each volume, all myelinated A $\beta$  sensory neuron axons were reconstructed. Also, a subset of small diameter neurons that innervated the hair follicle and Meissner corpuscle were reconstructed. Additional small diameter axons in the circumferential collagen were seen but their restricted innervation pattern was dissimilar to the anatomical characteristics of the A $\delta$  circ-HTMR. The terminal Schwann cells that associated with the lanceolate endings in the MH200121-B2K (guard hair follicle volume) and the lamellar cells that associated with the A $\beta$  sensory axons in the 200913FPT2 (dual-innervated Meissner corpuscle volume) were reconstructed to visualize the intimate interactions between the non-neuronal cells of the end organs and the A $\beta$  sensory axons. Additionally, we reconstructed a subset of the circumferential terminal Schwann cells that associated with the A $\beta$  field-LTMRs (this subset represents the majority of circumferential terminal Schwann cells in the volume) and a subset of previously uncharacterized circumferential support cells (CSCs) because of their numerous contacts with the protrusions of the A $\beta$  sensory axons of the hair follicle. Based on structural homology, we estimate there to be roughly 17 total CSCs with cell bodies that reside in the circumferential collagen matrix on the same horizontal plane as the lanceolate endings. Additional non-neuronal cells were observed in the volume but were not reconstructed. All single sections from FIB-SEM volumes presented in the paper are pseudo-colored by the trained networks.

### Immunoelectron microscopy sample preparation

Skin regions enriched for Meissner corpuscles, hair follicles, and Pacinian corpuscles were isolated from *Piezo2<sup>smFP-FLAG</sup>* mice or littermate controls. The *Plp1<sup>EGFP</sup>* allele was also present in all mice to aid sample preparation. Forepaw digit tips were isolated as described above. For back hairy skin, all hairs were trimmed short, and a rectangular piece of skin ( $\sim 1 \text{ mm} \times 2 \text{ mm}$ ) was dissected with the rostral/caudal axis oriented along the long axis of the sample. Pacinian corpuscles were isolated as described above. Samples were drop fixed in 4% PFA in 0.1 M phosphate buffer (PB) for 2 h at room temperature. Samples were micro-dissected 1 h into fixation to remove excess fat and muscle and returned to fix for the remainder of the 2 h.

After samples were washed in 0.1 M PB, they were cryoprotected in 30% sucrose in 0.1 M PB. Samples were then embedded in Neg-50 Frozen Section Medium (VWR, cat. no. 21008-918). Immediately after the samples were embedded, they were cryosectioned into  $50 \mu\text{m}$  sections and placed into chilled 0.1 M PB. *Plp1<sup>EGFP</sup>* mice were used to visualize and isolate sections with end organ structures. Sections were then incubated in 50 mM glycine in 0.1 M PB for 30 min. After aldehyde quenching, sections were blocked in 10% normal goat serum (Vector labs, cat. no. S-1000), 0.5% fish gelatin (Sigma, cat. no. G7041), and 0.05% Triton X-100 in 0.1 M PB for 2 h at room temperature. Sections were then incubated with primary antibody in a modified blocking solution—10% normal goat serum, 0.5% fish gelatin, 1:100 guinea pig anti-FLAG<sup>68</sup> in 0.1 M PB—for 24 h at room temperature under gentle agitation. After a



series of washes in 0.1 M PB, sections were incubated overnight with species-specific gold-labeled secondary antibody in a modified blocking solution—10% normal goat serum, 0.5% fish gelatin, 1:50 Nanogold-Fab' goat anti-guinea pig IgG (Nanoprobes, cat. no. 2055) in 0.1 M PB. After washes in 0.1 M PB, sections were post-fixed with 1% glutaraldehyde for 10 min before being thoroughly rinsed with dH<sub>2</sub>O.

To reveal gold labeling, sections were incubated with HQ Silver Enhancement (Nanoprobes, cat. no. 2012) for 8 min under gentle agitation. The enhancement reaction was quenched by the addition and subsequent rinses with dH<sub>2</sub>O. Following silver staining, samples were stained with 1% osmium tetroxide in 0.1M PB for 30 min and subsequently 1% uranyl acetate in 0.05 M maleate buffer overnight at 4°C. Sections were then dehydrated with serial ethanol and propylene oxide (VWR, cat. no. 20411) dilutions before infiltration and embedding in an epoxy resin (LX-112, Ladd Research) mix and cured at 60°C for 48–72 h. Ultrathin sections were cut at 50–70 nm and imaged using a JEOL 1200EX transmission electron microscope at 80 kV accelerating voltage. Images were cropped and adjusted to enhance contrast using Fiji/ImageJ.

### Quantification of immunoelectron microscopy signal

To quantify immunoelectron microscopy signal as enhanced by silver staining, the “Analyze Particles” function of Fiji/ImageJ was applied to 4–6 representative thresholded images selected for each animal. After properly setting the pixel-to-micron scale, images were uniformly cropped to exclude the attached metadata and smoothed to limit any static-like background signal. In all tissue types, the axon membrane was carefully traced in a freehand selection to include any overlying puncta and saved as a region of interest (ROI). The same was done for the surrounding lamellar cells in the lanceolate complexes and Meissner corpuscles, however, the increased lamellar complexity and decreased ultrastructural resolution prevented such an analysis of lamellar cells in the Pacinian corpuscles. These ROIs were shrunk by 80 nm, and the resulting ROIs were considered to be the “internal” ROIs of the lamellar or axon profiles, and the 80 nm-thick, nonoverlapping region between the external and internal ROIs was considered to be the membrane. In the analysis of all images, the membrane thickness was maintained as 80 nm to include the majority of large, membrane-associated puncta without including clearly internal puncta. The extracellular space of lanceolate and Meissner images was isolated by selecting the inverse of the axon, lamellar cells, and any other cells. Due to the increased lamellar cell complexity, density and decreased ultrastructural resolution of sections taken from the Pacinian corpuscle, the entire image, excluding the axon membrane and internal axon was categorized as “other.”

With ROIs made for analysis, the image was then thresholded with a minimum of 0 and maximum of 90, such that only the dark puncta were visible. The maximum of 90 was chosen, as any lower reduced the size of the puncta, and any higher included non-puncta relatively dark components of the image or background. Some images required adjustment of exposure or threshold to ensure that puncta were accurately captured. This thresholding process occasionally left dark spots of tears or particulates that were manually excluded from analyzed ROIs. The “Analyze Particles” function was then used on the ROIs corresponding to the axon membrane, internal axon, lamellar membrane, internal lamellar, extracellular space, and, with the Pacinian images, non-axonal space with a minimum size of 0.1 square nanometers to exclude any remaining static-like noise. For plotting, we used the automatically generated output average for puncta size and percent of ROI occupied by puncta (puncta area divided by ROI area).

### Quantification of lamellar cell wrappings

Six and nine imaging planes distributed through the single-innervated Meissner corpuscle and the dual-innervated Meissner corpuscle, respectively, were selected for lamellar cell wrapping analysis. A line was drawn through the center of each A $\beta$  sensory axon profile for each imaging plane. The line extended to the boundary of lamellar cell processes appearing to associate with each individual axon profile. The number of lamellar cell processes crossing that line were used to determine the number of lamellar cell processes wrapping that particular axon profile. This analysis is similar to previously described work.<sup>3</sup>

### Protrusion ending quantification

To characterize the terminal properties of axon protrusions, the final 50% of a protrusion was examined to assess whether it formed a contact (<30 nm of space between membranes) with another cell. In the hair follicle volume, protrusions along the A $\beta$  RA-LTMRs were categorized as terminating either in the local longitudinal collagen matrix or in the more distal circumferential collagen network. If a protrusion extended into the circumferential collagen network and came within ~30 nm of a terminal Schwann cell that was also within the circumferential collagen, then it was counted as a contact with a cell in the circumferential collagen. Protrusions were also counted along the A $\beta$  field-LTMRs. Small bumps along the sensory axons were not counted as protrusions. The same metrics were used to characterize the axon protrusions within both Meissner corpuscle FIB-SEM volumes. Because of the large size of the Pacinian corpuscle and the density of protrusions, we counted the number of protrusions and characterized their terminal endings in representative regions of the corpuscle and used that quantification to estimate the total number of protrusions and their terminal structures within the terminal and ultraterminal region of the Pacinian corpuscle. Two different regions in the terminal and ultraterminal region were selected to characterize protrusions to ensure we captured as much heterogeneity in protrusion density and terminal structure as possible across this large structure.

### Morphometric analysis of axon protrusions

We analyzed the morphometric properties (length and surface area) using the NeuroMorph 3D analysis toolkit<sup>72,73</sup> in Blender for a subset of representative protrusions distal to the branchpoint for each particular protrusion across each end organ type (<https://neuromorph.epfl.ch/>). The 3D meshes of the A $\beta$  LTMR lanceolate endings of the guard hair follicle volume, Ret<sup>+</sup> and TrkB<sup>+</sup> axons of the dual-innervated Meissner corpuscle volume, and the single A $\beta$  LTMR sensory axon of the Pacinian corpuscle volume were imported into Blender. In Blender, meshes were remeshed with the 'smooth' setting at an octree depth of 12. The meshes were then decimated to a value of 0.01 for the hair follicle and Meissner corpuscle volume and 0.2 for the Pacinian corpuscle volume, resulting in meshes with reduced face counts but with minimal changes to the overall shape of the mesh. NeuroMorph was then used to calculate the length of protrusions by selecting a vertex at the tip of the protrusion and the base (where axon protrusion merges with axon body or branches) and using the 'shortest distance along mesh' function. To calculate surface area, all faces along the protrusion (from tip to base/branch point) were selected and the measurements tool was used to calculate surface area.

### In vivo DRG electrophysiology

Juxtacellular recordings were made from DRG neurons *in vivo*. Mice of both sexes were anesthetized with urethane (1.5 g/kg). An incision was made over the lumbar spine and scalp. A headplate was fixed to the skull using cyanoacrylate adhesive. The muscle overlying the DCN was removed, and the dorsal aspect of the C1 vertebrae was removed. The L4 DRG was exposed and two custom made spinal clamps fixed the spine in place. A platinum-iridium bipolar stimulus electrode (FHC) was lowered into the caudal DCN or C1 DC. A glass electrode (borosilicate, 1–2 M $\Omega$ ) filled with saline was lowered into the DRG. Electrical stimuli (25–300  $\mu$ A, 0.2 ms duration) were delivered to the DCN/DC at 0.5–1 Hz while searching for a unit. Once an antidromically activated unit was isolated, the receptive field was determined by brushing the hindlimb and thigh. If no receptive field could be identified, a series of stimuli were systematically delivered to the hindpaw and thigh to search for activation. Once the receptive field was located, one of three stimuli were delivered. Air puffs (5 PSI from a 20 gauge needle, 1–3 mm from the hair) were used for hairy skin. For glabrous skin, a custom-built mechanical stimulator delivered static indentations (0–25 mN) using a 0.2 mm diameter probe tip. In some cases, vibration (10–1000 Hz, 0–25 mN) was delivered using the same stimulator. Signals were amplified using a Multiclamp 700A/B and acquired using a Digidata 1550A/B using Clampex 10/11 software. For A $\beta$  RA-LTMRs shown in Figure S1A, cells were visualized under a microscope in BAC-transgenic *NPY2R-GFP* mice<sup>8</sup> and large glass electrodes (20–30  $\mu$ m tip diameter) were used to perform targeted recordings as previously described.<sup>3</sup> Force indentations (0.5 s duration 1–75 mN intensity) and sine vibrations of varying frequency and intensity were used to characterize the response properties of five NPY2R-GFP<sup>+</sup> cells isolated from four animals. Similar responses were observed for all isolated cells.

### DRG electrophysiology analysis

Units that were antidromically identified from DCN/DC stimulation were sorted into categories based on their response properties. Units that had their mechanical receptive field on hairy skin and were activated by movement of hairs were classified as either 'guard hair A $\beta$  RA-LTMR' or 'limb hair A $\beta$  RA-LTMR', depending on their responses to deflection of different hair types. Units that had receptive fields on glabrous skin were classified as either 'Meissner A $\beta$  RA-LTMR' or 'A $\beta$  SA-LTMR' depending on their adaptation properties. Units that did not have a cutaneous receptive field but could become phase-locked to high frequency vibration (>300 Hz) were classified as 'Pacinian A $\beta$  RA-LTMR'. Units were also detected that specifically responded to mechanical stimulation of the toenail and were classified as 'toenail A $\beta$  RA-LTMR'. These units also phase-locked to high frequency vibration (300 Hz). Units that lacked a specific cutaneous receptive field, but responded strongly to bending of the toe were identified as 'proprioceptor'. If units in any animal did not respond to air puff, brush, or strong vibration delivered to the thigh, trunk, or hindlimb, the units were classified as 'insensitive'.

In *Cdx2<sup>Cre</sup>; Piezo<sup>fl/m</sup>* animals receptive fields were not discernable by brushing. Air puffs and brushes were delivered systematically across the hindlimb and thigh. The hindlimb was pinched if no mechanically evoked responses could be found in order to confirm that the nerve from the DRG to the periphery was not damaged. Pinching in some cases evoked firing in antidromically-identified units, but in many recordings pinch-activated units were not activated by DCN/DC stimulation.

### Open field and balance beam behavior analysis

**Open Field Test:** Two days prior to open field testing animals were moved to the testing room and home cage habituated to the behavior room to acclimate to room lighting, sound, odor and temperature. Animals were habituated to investigator handling by undergoing tail inking. On the third day following room habituation each animal was placed in a black matte acrylic Open field chamber (25 cm  $\times$  25 cm) and allowed to freely explore for 5 min. A top video recording was used to track distance traveled and generate movement trace maps of each animal.

**Balance Beam Test:** The balance beam was constructed of a 1 m matte white acrylic bar with a flat 12 mm surface. The beam was mounted ~50 cm above the bench top. A black matte acrylic box was placed at each end of the beam to provide a start and end enclosure for the animal. A soft pad was stretched below the beam to serve as a soft landing surface to cushion falls. A digital USB 2.0 CMOS video camera was mounted above the balance beam to record crossings.

One hour prior to training and testing animals were habituated to the behavior room to acclimate to room lighting, sound, odor and temperature and investigator handling by undergoing tail inking. To train the animals to cross freely, each animal was placed on the

beam and encouraged to cross at least 3 times before returning to the home cage. If animals refused to cross, the investigator gently touched the hindquarters to encourage forward movement. Animals habituated and trained to freely cross the beam were then tested and 4 beam crossings were video recorded. Each animal was allowed to rest for no more than 10 s between each crossing. The animals were then returned to their home cage once 4 successful trials were completed. Time to cross beam was analyzed. The *Cdx2<sup>Cre</sup>*; *Piezo2<sup>fl/fl</sup>* or *fl<sup>null</sup>* animals were not run on the balance beam because of their poor motor coordination.

#### QUANTIFICATION AND STATISTICAL ANALYSIS

Statistical analysis was performed using Prism. All statistically tests performed are indicated in the figure legends.  $p < 0.05$  was considered significant. Both non-parametric tests and parametric tests were used, depending on data normality. Additional details on sample sizes and statistical tests for each experiment can be found in the figure legends and main text.

#### ADDITIONAL RESOURCES

Illustrations were designed in Adobe Illustrator and Biorender ([Biorender.com](https://biorender.com)).